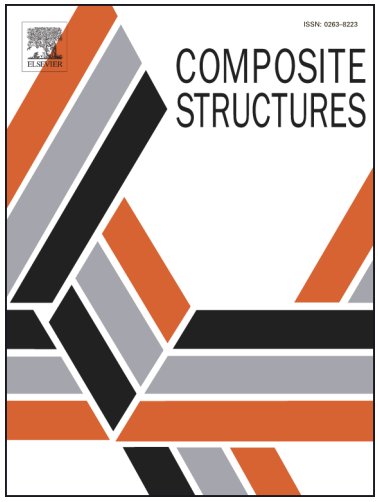

Thermo-mechanical post-buckling analysis of variable angle tow composite plate assemblies

V. Oliveri, A. Milazzo, P.M. Weaver

PII: S0263-8223(17)30787-0
DOI: http://dx.doi.org/10.1016/j.compstruct.2017.07.050
Reference: COST 8705

To appear in: *Composite Structures*

Please cite this article as: Oliveri, V., Milazzo, A., Weaver, P.M., Thermo-mechanical post-buckling analysis of variable angle tow composite plate assemblies, *Composite Structures* (2017), doi: http://dx.doi.org/10.1016/j.compstruct.2017.07.050

Thermo-mechanical post-buckling analysis of variable angle tow composite plate assemblies

V. Oliveri[a,*], A. Milazzo[b], P. M. Weaver[a]

[a] *Bernal Institute, School of Engineering, University of Limerick, Limerick, Ireland*
[b] *Dipartimento di Ingegneria Civile, Ambientale, Aerospaziale, dei Materiali, University of Palermo, Viale delle Scienze, Bldg 8, 90128 Palermo - Italy*

Abstract

The increasing use of composite materials for lightweight structural applications and the extended tailoring capabilities offered by variable stiffness laminates requires rapid and robust analysis tools that adequately describe the mechanical behaviour of such structures. In this work, a Rayleigh-Ritz solution for generally restrained multilayered stiffened variable angle tow plates in the post-buckling regime is presented. The plate model is based on first-order shear deformation theory and accounts for geometrical nonlinearity through von Kármán's assumptions. General symmetric and unsymmetric stacking sequences are considered and Legendre orthogonal polynomials are employed to approximate the unknown displacement field. Stiffened variable angle tow plates are modeled as an assembly of plate-like elements and penalty techniques are used to enforce the displacements continuity of the assembled multidomain structure and also to apply the kinematical boundary conditions. The developed postbuckling analysis is sufficiently versatile to model a wide range of configurations and load cases for multi-component, variable angle tow, composite structures, and provide the same accuracy level as finite element analysis. The proposed solution is validated by comparison with literature and finite elements analysis and original results are presented for the thermo-mechanical post-buckling solution

*Corresponding author. Tel.: +353 87 096 2987
Email addresses: vincenzo.oliveri@ul.ie (V. Oliveri), alberto.milazzo@unipa.it (A. Milazzo), paul.weaver@ul.ie (P. M. Weaver)

of multilayered stiffened variable angle tow plates. The effectiveness of the developed analysis tool for both stiffened plates and a tapered stiffened wing box is shown, with a reduced number of unknowns and simplified data preparation compared to finite element analysis.

1. Introduction

The excellent mechanical properties offered by fibre-reinforced laminates have driven their application as components of advanced and lightweight structures. Widely employed in automotive, naval and aerospace applications, composite laminates are often designed as stiffened panels or thin-walled structures. These structures are able to sustain mechanical loads well beyond the occurrence of buckling and thus, are especially suited for aerospace applications where weight is crucially important. As such, the accurate analysis of multilayered composite plate postbuckling regime becomes highly relevant in the design process to increase weight savings and improve safety margins.

The introduction of variable angle tow (VAT) composites [1, 2] provides new ways to design high performance composite structures. We distinguish VAT composites from the more general functionally graded materials. The former vary their properties continuously in-plane and discretely through-thickness whilst the latter vary their properties continuously, with most applications considering variations in thickness only. The development of such VAT laminates redefines the tailoring concept by distributing layups with certain fibre orientations across the planform of the plate, as well as through the thickness. This approach can improve structural performance: for example, VAT composite plates undergoing compression loads showed an improvement up to 50% of buckling load over conventional straight fibre composites [3].

This new class of advanced composite structure requires new modelling techniques that should not only be able to capture their complex responses but also do so relatively simply so that these models form tools that can be subsequently used for efficient and safe design purposes. The Rayleigh-Ritz method

is one of the most successful approaches to describe the buckling and post-buckling behaviour of composite plates that can also be implemented with high computational efficiency [4–7]. Rayleigh-Ritz solutions for static loading, free vibrations, buckling and postbuckling analysis of composite plates have been proposed. However, most of the proposed Rayleigh-Ritz solutions implement classical laminated plate theory (CLPT) [8–13] that only applies to relatively thin plates, therefore neglecting transverse shear strains, which can play an important role in thick plates or low transverse shear stiffness structures. First-order shear deformation theory (FSDT) is adequate for the engineering analysis and design of most thin to moderately thick composite laminates [6] and it is appealing compared with more sophisticated higher order plate theories, due to its simplicity and low computational costs.

Focusing on FSDT modelling of plates solved by the Rayleigh-Ritz method, different kinds of trial function have been proposed, showing reliable results for static analysis [14, 15], free vibrations [16–21], buckling [14, 16] and postbuckling [22–24] of thin to moderately thick composite laminated plates. Adopting classical thin plate theory, the Rayleigh-Ritz method has also been used also to analyze the buckling and postbuckling behaviour of stiffened plates [8–13] and shells [25, 26]. Regarding variable stiffness composite plates, starting from the pioneering works by Gürdal and Olmedo [2], attention has been devoted to VAT composites as demonstrated by the recent literature on the subject [27–38]. These works show that most of the research on VAT composites has been carried out for buckling and is almost limited to flat or cylindrical configurations modeled by CLPT. Few results are available for FSDT modelling [39, 40] and for stiffened panels [41, 42]. To the best of the authors' knowledge, the postbuckling behaviour of VAT stiffened composite plates remains unexplored.

Recently, the lead authors of the present work presented a Rayleigh-Ritz approach for large deflection analysis of composite panels and thin-walled structures based on FSDT [43–45], demonstrating its ability in modelling postbuckling behaviour. In the present study, this approach is extended to VAT stiffened plates and thin-walled structures undergoing thermo-mechanical loadings. In

particular, a Rayleigh-Ritz solution for generally restrained, multilayered stiffened VAT panels in the postbuckling regime is presented. Stiffened VAT plates are modelled as an assembly of plate-like elements, over which a varying fibre orientation angle is considered. The plate model is based on first-order shear deformation theory and accounts for geometrical nonlinearity through von Kármán's assumptions. Penalty techniques are used to enforce displacement continuity of the multidomain assembled structure and also to apply kinematical boundary conditions. Legendre orthogonal polynomials are employed to approximate the unknown displacement field due to their known excellent properties for capturing local responses with few terms [46]. Subsequently, a computer code was developed to implement the corresponding Rayleigh-Ritz solution for thermomechanical postbuckling analysis of stiffened composite VAT plates with general configurations and loadings. Finally, validation and original results are presented for stiffened plates as well as a tapered, stiffened wingbox representative of a medium range aircraft. Our aim is to verify the applicability of the approach based on the Rayleigh-Ritz method and domain decomposition to the study of complex VAT structures in the postbuckling regime, ascertaining the accuracy, effectiveness and computational cost of the proposed analysis tool.

2. Formulation

2.1. Modelling strategy and definitions

The proposed modelling strategy treats the entire multi-part structure as an assembly of plate-like subdomains, referred in the following as plates or elements, and applying first-order shear deformation theory to obtain the governing equations of each multilayered plate as a single separate entity. In turn, the entire thin-walled structure is assembled by enforcing the boundary conditions for each component; these are given by displacement continuity and traction equilibrium along the edges joining different elements and by the external load and kinematical constraint conditions.

Consider a thin-walled structure treated as an assembly of N_P quadrilateral composite multilayered plates and let the superscript k inside angle bracket denote quantities associated with the k-th element. Each plate can be kinematically constrained on the lateral boundary and it is subjected to domain and boundary loads as specified in the next Section. The k-th plate is referred to its own local cartesian coordinate system with the origin located at the plate centre whose $x_3^{\langle k \rangle}$ axis is directed along the plate thickness whereas the $x_1^{\langle k \rangle}$ and $x_2^{\langle k \rangle}$ coordinates span the mid-plane. Let the domain occupied by the plate mid-plane be denoted by $\Omega^{\langle k \rangle}$ with $\partial\Omega^{\langle k \rangle}$ as its boundary. The whole structure is also referred to a global cartesian coordinate system whose axes are denoted by X_i. To deal with arbitrary shaped quadrilateral plates, let us introduce a natural coordinate system $\xi^{\langle k \rangle}\eta^{\langle k \rangle}$, which maps the plate mid-plane coordinates to the square domain $[-1,1]\times[-1,1]$. The plate's in-plane coordinates become

$$x_i^{\langle k \rangle} = \sum_{\alpha=1}^{4} g_\alpha(\xi^{\langle k \rangle}, \eta^{\langle k \rangle})\, x_{i\alpha}^{\langle k \rangle} \qquad i = 1,\ 2 \tag{1}$$

where $x_{i\alpha}^{\langle k \rangle}$ are the coordinates of the α-th vertex of the plate's mid-plane along the i-th axis and

$$g_1 = \frac{1}{4}(1-\xi)(1-\eta) \tag{2a}$$

$$g_2 = \frac{1}{4}(1+\xi)(1-\eta) \tag{2b}$$

$$g_3 = \frac{1}{4}(1+\xi)(1+\eta) \tag{2c}$$

$$g_4 = \frac{1}{4}(1-\xi)(1+\eta) \tag{2d}$$

2.2. Isolated plate governing equations

Now consider the k-th plate of the thin-walled structure as an isolated structural entity. In this subsection, the superscript $\langle k \rangle$ is omitted to simplify visual complexity, but is restored later when relevant for the formulation development. Referring to the local cartesian coordinate system x_i and employing FSDT, the plate deformation is described by the displacement vector $\boldsymbol{d} = \{\, d_1 \;\; d_2 \;\; d_3 \,\}^T$, expressed as

$$\boldsymbol{d} = \boldsymbol{u} + (x_3 + \bar{x}_3)\, \boldsymbol{L}\, \boldsymbol{\vartheta} + \bar{\boldsymbol{w}} \tag{3}$$

where

$$\boldsymbol{L} = \begin{bmatrix} 1 & 0 & 0 \\ 0 & 1 & 0 \\ 0 & 0 & 0 \end{bmatrix} \tag{4}$$

and $\bar{x}_3$ is the offset that defines the so called modelling plane $x_3 = -\bar{x}_3$. In Eq. (3), denoting the displacement components of the $\bar{x}_3$-plane points along the reference directions by $u_1 = u_1(\xi, \eta)$, $u_2 = u_2(\xi, \eta)$ and $u_3 = u_3(\xi, \eta)$, then $\boldsymbol{u} = \{u_1 \;\; u_2 \;\; u_3\}^T$ and $\boldsymbol{\vartheta} = \{\vartheta_1 \;\; \vartheta_2 \;\; \vartheta_3\}^T$ where $\vartheta_1 = \vartheta_1(\xi, \eta)$ and $\vartheta_2 = \vartheta_2(\xi, \eta)$ are the rotations of the transverse normal around the x_2 and x_1 axes, respectively, and $\vartheta_3 = \vartheta_3(\xi, \eta)$ is the "drilling" rotation. Note that the drilling rotation does not affect the plate deformation and its introduction relates to the enforcement of the interface conditions along the edges joining different plates [47] as described in Section 2.3. To consider initial imperfections of the structure, Eq. (3) accounts for the term $\bar{\boldsymbol{w}} = \left\{0 \quad 0 \quad \bar{w}\right\}^T$ where $\bar{w}$ is a prescribed initial transverse deflection of the plate's modelling plane. Referring to non-isothermal conditions, we also introduce the temperature increment $\Delta T = \Delta T(x_1, x_2, x_3)$ as the temperature increment of the plate from a reference state, that is

$$\Delta T = T - T_{ref} \tag{5}$$

Assuming that the temperature increment varies linearly, in order to be consistent with the assumed displacement field, one has

$$\Delta T = T_0 + (x_3 + \bar{x}_3)\, T_1 \tag{6}$$

where $T_0 = T_0(x_1, x_2)$ is the temperature increment of the plate's modelling plane and $T_1 = T_1(x_1, x_2)$ is its variation across the plate thickness.

Adopting the total Lagrangian formulation and assuming moderately large displacements, the kinematical state is described by Green's strain vector [48] $\boldsymbol{e}$ that is partitioned into the in-plane and out-of-plane component vectors denoted by the subscripts p and n, respectively

$$\boldsymbol{e} = \{\, e_{11} \;\; e_{22} \;\; e_{12} \,|\, e_{13} \;\; e_{23} \;\; e_{33} \,\}^T = \left\{ \begin{array}{c} \boldsymbol{e}_p \\ \boldsymbol{e}_n \end{array} \right\} \tag{7}$$

Taking geometric nonlinearity in to account through von Kármán's assumptions, the mechanical strain-displacement relations are given by

$$\begin{aligned} \boldsymbol{e}_p &= \boldsymbol{\mathscr{D}}_p \boldsymbol{u} + \frac{1}{2} (\boldsymbol{\mathscr{D}}_p \otimes u_3)\, \boldsymbol{\mathscr{D}}_n \boldsymbol{u} + \\ &\qquad (\boldsymbol{\mathscr{D}}_p \otimes \bar{w})\, \boldsymbol{\mathscr{D}}_n \boldsymbol{u} + (x_3 + \bar{x}_3)\, \boldsymbol{\mathscr{D}}_p \boldsymbol{\vartheta} \\ &= \boldsymbol{\varepsilon}_0 + (x_3 + \bar{x}_3)\, \boldsymbol{\kappa} \end{aligned} \tag{8a}$$

$$\boldsymbol{e}_n = \boldsymbol{\mathscr{D}}_n \boldsymbol{u} + \boldsymbol{L}\boldsymbol{\vartheta} = \boldsymbol{\gamma} \tag{8b}$$

where the in-plane strain vector $\boldsymbol{\varepsilon}_0$, the curvature vector $\boldsymbol{\kappa}$ and shear strain vector $\boldsymbol{\gamma}$ are introduced together with the differential operators

$$\boldsymbol{\mathscr{D}}_p = \begin{bmatrix} \frac{\partial}{\partial x_1} & 0 & 0 \\ 0 & \frac{\partial}{\partial x_2} & 0 \\ \frac{\partial}{\partial x_2} & \frac{\partial}{\partial x_1} & 0 \end{bmatrix} \tag{9a}$$

$$\boldsymbol{\mathscr{D}}_n = \begin{bmatrix} 0 & 0 & \frac{\partial}{\partial x_1} \\ 0 & 0 & \frac{\partial}{\partial x_2} \\ 0 & 0 & 0 \end{bmatrix} \tag{9b}$$

Substituting Eq. (1) into Eq. (9) gives

$$\frac{\partial}{\partial x_1} = \frac{1}{J_{11}J_{22} - J_{12}J_{21}} \left(J_{22}\frac{\partial}{\partial \xi} - J_{12}\frac{\partial}{\partial \eta} \right) \tag{10a}$$

$$\frac{\partial}{\partial x_2} = \frac{1}{J_{11}J_{22} - J_{12}J_{21}} \left(-J_{21}\frac{\partial}{\partial \xi} + J_{11}\frac{\partial}{\partial \eta} \right) \tag{10b}$$

where $J_{\alpha\beta}$ are the elements of the Jacobian matrix associated with the coordinate transformation.

The mechanical state is expressed by the plate's internal actions, namely membrane stress resultants per unit length $\boldsymbol{N}$, moments per unit length $\boldsymbol{M}$, and transverse stress resultants per unit length $\boldsymbol{T}$ which are defined through suitable integration of the stresses over the plate thickness. The constitutive relationships of the plate are [48]

$$\begin{Bmatrix} \boldsymbol{N} \\ \boldsymbol{M} \\ \boldsymbol{T} \end{Bmatrix} = \begin{bmatrix} \boldsymbol{A}_p & \boldsymbol{B} & \boldsymbol{0} \\ \boldsymbol{B} & \boldsymbol{D} & \boldsymbol{0} \\ \boldsymbol{0} & \boldsymbol{0} & \boldsymbol{A}_n \end{bmatrix} \begin{Bmatrix} \boldsymbol{\varepsilon}_0 \\ \boldsymbol{\kappa} \\ \boldsymbol{\gamma} \end{Bmatrix} - \begin{Bmatrix} \boldsymbol{N}_{\Delta T} \\ \boldsymbol{M}_{\Delta T} \\ \boldsymbol{0} \end{Bmatrix} \tag{11}$$

where the generalized thermal stresses $\boldsymbol{N}_{\Delta T}$ and $\boldsymbol{M}_{\Delta T}$ are given by

$$\boldsymbol{N}_{\Delta T} = \sum_{i=1}^{N_l} \int_{h_{i-1}}^{h_i} \boldsymbol{Q}_{p_i}\, \boldsymbol{\alpha}_i\, \Delta T\, dx_3 \tag{12a}$$

$$\boldsymbol{M}_{\Delta T} = \sum_{i=1}^{N_l} \int_{h_{i-1}}^{h_i} (x_3 + \bar{x}_3)\, \boldsymbol{Q}_{p_i}\, \boldsymbol{\alpha}_i\, \Delta T\, dx_3 \tag{12b}$$

and the generalized stiffness matrices $\boldsymbol{A}_p$, $\boldsymbol{B}$, $\boldsymbol{D}$ and $\boldsymbol{A}_n$ are defined as

$$\boldsymbol{A}_p = \sum_{i=1}^{N_l} \int_{h_{i-1}}^{h_i} \boldsymbol{Q}_{p_i} dx_3 \tag{13a}$$

$$\boldsymbol{B} = \sum_{i=1}^{N_l} \int_{h_{i-1}}^{h_i} (x_3 + \bar{x}_3)\, \boldsymbol{Q}_{p_i} dx_3 \tag{13b}$$

$$\boldsymbol{D} = \sum_{i=1}^{N_l} \int_{h_{i-1}}^{h_i} (x_3 + \bar{x}_3)^2\, \boldsymbol{Q}_{p_i} dx_3 \tag{13c}$$

$$\boldsymbol{A}_n = \sum_{i=1}^{N_l} \int_{h_{i-1}}^{h_i} \boldsymbol{Q}_{n_i} dx_3 \tag{13d}$$

In Eqs. (12) and Eqs. (13), N_l is the number of laminate plies whereas h_{i-1} and h_i are the bottom and top face x_3 coordinates of the i-th ply, respectively. The 3×1 vectors $\boldsymbol{\alpha}_i$ contain the transformed thermal coefficients of expansion and the 3×3 matrices $\boldsymbol{Q}_{p_i}$ and $\boldsymbol{Q}_{n_i}$ contain the ply stiffness coefficients. Note that the ply stiffness matrices as well as the thermal coefficients of expansion depend on the fibre orientation θ of each ply that for VAT composite plates can be considered as a function of the in-plane coordinates of each layer, namely $\theta = \theta\,(x_1, x_2)$.

The external loads and constraint reactions of the k-th plate consist of the forces $\boldsymbol{q} = \begin{Bmatrix} q_1 & q_2 & q_3 \end{Bmatrix}^T$ and moments $\boldsymbol{m} = \begin{Bmatrix} m_1 & m_2 & 0 \end{Bmatrix}^T$ per unit area applied over the domain Ω and the resultant forces $\tilde{\boldsymbol{N}} = \begin{Bmatrix} \tilde{N}_1 & \tilde{N}_2 & \tilde{N}_3 \end{Bmatrix}^T$ and moments $\tilde{\boldsymbol{M}} = \begin{Bmatrix} \tilde{M}_1 & \tilde{M}_2 & 0 \end{Bmatrix}^T$ per unit length applied on the boundary $\partial\Omega$. On the loaded part of the plate boundary $\partial\Omega_l$,

$$\tilde{\boldsymbol{N}} = \bar{\boldsymbol{N}} \quad \text{on } \partial\Omega_l \tag{14a}$$

$$\tilde{\boldsymbol{M}} = \bar{\boldsymbol{M}} \quad \text{on } \partial\Omega_l \tag{14b}$$

where the overbar denotes prescribed quantities.

The essential boundary conditions are provided prescribing the generalized displacements on the part $\partial\Omega_c$ of the boundary,

$$\boldsymbol{\Xi}_u \boldsymbol{u} = \boldsymbol{\Xi}_u \bar{\boldsymbol{u}} \quad \text{on } \partial\Omega_c \tag{15a}$$

$$\boldsymbol{\Xi}_\vartheta \boldsymbol{\vartheta} = \boldsymbol{\Xi}_\vartheta \bar{\boldsymbol{\vartheta}} \quad \text{on } \partial\Omega_c \tag{15b}$$

where, again, the overbar denotes prescribed quantities and $\boldsymbol{\Xi}_u$ and $\boldsymbol{\Xi}_\vartheta$ are suitable Boolean matrix operators that select the constrained components of the generalized displacements vectors. Note that Eqs. (15) gives the trivial zero identity for unconstrained generalized displacement components.

As the governing equations are deduced through the Principle of Minimum Total Potential Energy, the total energy of the plate is given by the sum of the strain energy of the plate and work done by external loads by

$$\begin{aligned}\Pi = \int_\Omega \frac{1}{2}\Big[&{\boldsymbol{\varepsilon}_0}^T \boldsymbol{A}_p \boldsymbol{\varepsilon}_0 + {\boldsymbol{\varepsilon}_0}^T \boldsymbol{B}\boldsymbol{\kappa} + \boldsymbol{\kappa}^T \boldsymbol{B}\boldsymbol{\varepsilon}_0 + \\ &\boldsymbol{\kappa}^T \boldsymbol{D}\boldsymbol{\kappa} + \boldsymbol{\gamma}^T \boldsymbol{A}_n \boldsymbol{\gamma}\Big] d\Omega - \\ \int_\Omega &\left[{\boldsymbol{\varepsilon}_0}^T \boldsymbol{N}_{\Delta T} + \boldsymbol{\kappa}^T \boldsymbol{M}_{\Delta T} + \boldsymbol{u}^T \boldsymbol{q} + \boldsymbol{\vartheta}^T \boldsymbol{m}\right] d\Omega - \\ \int_{\partial\Omega_l} &\left[\boldsymbol{u}^T \bar{\boldsymbol{N}} + \boldsymbol{\vartheta}^T \bar{\boldsymbol{M}}\right] d\partial\Omega - \\ \int_{\partial\Omega_c} &\left[\boldsymbol{u}^T \tilde{\boldsymbol{N}} + \boldsymbol{\vartheta}^T \tilde{\boldsymbol{M}}\right] d\partial\Omega\end{aligned} \tag{16}$$

2.3. Edge continuity conditions

Let Γ_{pq} be the common edge along with the two contiguous plates denoted by $\langle p\rangle$ and $\langle q\rangle$. The joining conditions along this edge require displacement continuity and tractions equilibrium. The displacement continuity on Γ_{pq} is implemented requiring that: (i) the modelling plane translations of the two contiguous plates have equal components in the global reference system, (ii) the rotations around the the global axes of the two contiguous plates are equal. These considerations give

$$\boldsymbol{\Lambda}_u^{\langle p\rangle} \boldsymbol{u}^{\langle p\rangle} = \boldsymbol{\Lambda}_u^{\langle q\rangle} \boldsymbol{u}^{\langle q\rangle} \qquad \text{on } \Gamma_{pq} \tag{17a}$$

$$\boldsymbol{\Lambda}_\vartheta^{\langle p\rangle} \boldsymbol{\vartheta}^{\langle p\rangle} = \boldsymbol{\Lambda}_\vartheta^{\langle q\rangle} \boldsymbol{\vartheta}^{\langle q\rangle} \qquad \text{on } \Gamma_{pq} \tag{17b}$$

where $\boldsymbol{\Lambda}_\alpha^{\langle r\rangle}$ are suitable transformation matrices from the local to the global reference systems, which contain the directional cosines between the axes X_i and $x_j^{\langle k\rangle}$. It is worth nothing that by introducing the drilling rotation, one assumes

that rotations around the local x_3-axis of the plate are admitted despite their non-influence on the plate deformation. This process allows all of the possible cases of edge rotation continuity to be treated by a single formula that is Eq. (17b). Indeed, in Eq. (17b) three-component rotations vectors are used and each rotation component of the first plate can match a correspondent rotation of the second plate [47]. For the case of an edge shared among multiple plates, Eqs. (17) are written for all possible coupled combinations of plates consisting of a fixed element and other ones.

As regards traction equilibrium, these reduce to the equilibrium of the boundary resultant forces and moments expressed in terms of their components along and around the global references axes, respectively. Therefore

$$\sum_j \boldsymbol{\Lambda}_u^{\langle j \rangle} \tilde{\boldsymbol{N}}^{\langle j \rangle} = \mathbf{0} \tag{18a}$$

$$\sum_j \boldsymbol{\Lambda}_\vartheta^{\langle j \rangle} \tilde{\boldsymbol{M}}^{\langle j \rangle} = \mathbf{0} \tag{18b}$$

where the summation involves all of the plates joined at the considered edge.

2.4. Variational statement and governing equations of the thin-walled structure

The governing equations of the whole structure are obtained by imposing the stationarity of its total potential energy under the constraints that joining and essential boundary conditions have to be satisfied. The total potential energy Π of the structure is recovered by summing the strain energy and the load potential of all of the plates. It is observed that, by virtue of the interface continuity conditions, the boundary loads along the common edge joining contiguous plates contribute overall zero work and thus the load potential of the whole structure involves the loads applied on external boundaries of plates only. The enforcement of the edge constraints in the problem variational statement is accomplished by introducing penalty terms associated with Eqs. (15) and (17) [49]. Therefore, the governing equations of the structure are formulated as the

free stationarity problem associated with the following functional

$$
\begin{aligned}
\mathit{\Pi} = & \sum_{k=1}^{N_P} \int_{\Omega^{\langle k \rangle}} \frac{1}{2} \Big[{\boldsymbol{\varepsilon}_0^{\langle k \rangle}}^T \boldsymbol{A}_p^{\langle k \rangle} \boldsymbol{\varepsilon}_0^{\langle k \rangle} + {\boldsymbol{\varepsilon}_0^{\langle k \rangle}}^T \boldsymbol{B}^{\langle k \rangle} \boldsymbol{\kappa}^{\langle k \rangle} + {\boldsymbol{\kappa}^{\langle k \rangle}}^T \boldsymbol{B}^{\langle k \rangle} \boldsymbol{\varepsilon}_0^{\langle k \rangle} + \\
& \qquad {\boldsymbol{\kappa}^{\langle k \rangle}}^T \boldsymbol{D}^{\langle k \rangle} \boldsymbol{\kappa}^{\langle k \rangle} + {\boldsymbol{\gamma}^{\langle k \rangle}}^T \boldsymbol{A}_n^{\langle k \rangle} \boldsymbol{\gamma}^{\langle k \rangle} \Big] d\Omega - \\
& \sum_{k=1}^{N_P} \int_{\Omega^{\langle k \rangle}} \left[{\boldsymbol{\varepsilon}_0^{\langle k \rangle}}^T \boldsymbol{N}_{\Delta T}^{\langle k \rangle} + {\boldsymbol{\kappa}^{\langle k \rangle}}^T \boldsymbol{M}_{\Delta T}^{\langle k \rangle} + {\boldsymbol{u}^{\langle k \rangle}}^T \boldsymbol{q}^{\langle \boldsymbol{k} \rangle} + {\boldsymbol{\vartheta}^{\langle k \rangle}}^T \boldsymbol{m}^{\langle k \rangle} \right] d\Omega - \\
& \sum_{k=1}^{N_P} \int_{\partial\Omega_l^{\langle k \rangle}} \left[{\boldsymbol{u}^{\langle k \rangle}}^T \bar{\boldsymbol{N}}^{\langle k \rangle} + {\boldsymbol{\vartheta}^{\langle k \rangle}}^T \bar{\boldsymbol{M}}^{\langle k \rangle} \right] d\partial\Omega + \\
& \sum_{k=1}^{N_P} \int_{\partial\Omega_c^{\langle k \rangle}} \frac{1}{2} \left[\boldsymbol{\Xi}_u^{\langle k \rangle} \boldsymbol{u}^{\langle k \rangle} - \boldsymbol{\Xi}_u^{\langle k \rangle} \bar{\boldsymbol{u}}^{\langle k \rangle} \right]^T \boldsymbol{\omega}_u^{\langle k \rangle} \left[\boldsymbol{\Xi}_u^{\langle k \rangle} \boldsymbol{u}^{\langle k \rangle} - \boldsymbol{\Xi}_u^{\langle k \rangle} \bar{\boldsymbol{u}}^{\langle k \rangle} \right] d\partial\Omega + \\
& \sum_{k=1}^{N_P} \int_{\partial\Omega_c^{\langle k \rangle}} \frac{1}{2} \left[\boldsymbol{\Xi}_\vartheta^{\langle k \rangle} \boldsymbol{\vartheta}^{\langle k \rangle} - \boldsymbol{\Xi}_\vartheta^{\langle k \rangle} \bar{\boldsymbol{\vartheta}}^{\langle k \rangle} \right]^T \boldsymbol{\omega}_\vartheta^{\langle k \rangle} \left[\boldsymbol{\Xi}_\vartheta^{\langle k \rangle} \boldsymbol{\vartheta}^{\langle k \rangle} - \boldsymbol{\Xi}_\vartheta^{\langle k \rangle} \bar{\boldsymbol{\vartheta}}^{\langle k \rangle} \right] d\partial\Omega \\
& \sum_{p=1}^{N_P-1} \sum_{q=p+1}^{N_P} \int_{\Gamma_{pq}} \frac{1}{2} \left[\boldsymbol{\Lambda}_u^{\langle p \rangle} \boldsymbol{u}^{\langle p \rangle} - \boldsymbol{\Lambda}_u^{\langle q \rangle} \boldsymbol{u}^{\langle q \rangle} \right]^T \boldsymbol{\omega}_u^{\langle p,q \rangle} \left[\boldsymbol{\Lambda}_u^{\langle p \rangle} \boldsymbol{u}^{\langle p \rangle} - \boldsymbol{\Lambda}_u^{\langle q \rangle} \boldsymbol{u}^{\langle q \rangle} \right] d\Gamma + \\
& \sum_{p=1}^{N_P-1} \sum_{q=p+1}^{N_P} \int_{\Gamma_{pq}} \frac{1}{2} \left[\boldsymbol{\Lambda}_\vartheta^{\langle p \rangle} \boldsymbol{\vartheta}^{\langle p \rangle} - \boldsymbol{\Lambda}_\vartheta^{\langle q \rangle} \boldsymbol{\vartheta}^{\langle q \rangle} \right]^T \boldsymbol{\omega}_\vartheta^{\langle p,q \rangle} \left[\boldsymbol{\Lambda}_\vartheta^{\langle p \rangle} \boldsymbol{\vartheta}^{\langle p \rangle} - \boldsymbol{\Lambda}_\vartheta^{\langle q \rangle} \boldsymbol{\vartheta}^{\langle q \rangle} \right] d\Gamma
\end{aligned}
\tag{19}
$$

where N_P is the number of plate-like elements used in the domain decomposition of the structure and $\boldsymbol{\omega}_u^{\langle k \rangle}$, $\boldsymbol{\omega}_\vartheta^{\langle k \rangle}$, $\boldsymbol{\omega}_u^{\langle p,q \rangle}$ and $\boldsymbol{\omega}_\vartheta^{\langle p,q \rangle}$ are diagonal matrices containing the penalty coefficients. It is noted that the joining constraints are algorithmically expressed considering all of the possible coupled combinations of plates in the structure through the double summation introduced in Eq. (19); if the plates $\langle p \rangle$ and $\langle q \rangle$ do not share a joining edge then Γ_{pq} has zero measure and thus the corresponding constraint actually become meaningless. Similar considerations hold for the essential boundary conditions constraints, which are introduced for all of the plates and give no contribution if $\partial\Omega_c^{\langle k \rangle}$ has zero measure.

The stationarity condition of the functional $\mathit{\Pi}$ can be investigated through standard calculus of variation procedures that provide a set of nonlinear equations governing the problem solution in terms of generalized displacements $\boldsymbol{u}^{\langle k \rangle}$ and $\boldsymbol{\vartheta}^{\langle k \rangle}$.

3. Rayleigh-Ritz solution

3.1. Kinematics approximation

To solve the stationary problem described in the preceding Section, a Rayleigh-Ritz solution scheme is adopted and the generalized displacements for each k-th plate are approximated as

$$u_j^{\langle k\rangle} = \sum_{i=0}^{N_{u_j}} \psi_i^{\langle k\rangle}\, C_{u_{j_i}}{}^{\langle k\rangle} = \boldsymbol{\Psi}_{u_j}^{\langle k\rangle} \boldsymbol{C}_{u_j}^{\langle k\rangle} \qquad j = 1,2,3 \tag{20a}$$

$$\vartheta_j^{\langle k\rangle} = \sum_{i=0}^{N_{\vartheta_j}} \psi_i^{\langle k\rangle}\, C_{\vartheta_{j_i}}{}^{\langle k\rangle} = \boldsymbol{\Psi}_{\vartheta_j}^{\langle k\rangle} \boldsymbol{C}_{\vartheta_j}^{\langle k\rangle} \qquad j = 1,2,3 \tag{20b}$$

where the $1 \times (N_\tau + 1)$ row vectors $\boldsymbol{\Psi}_\tau^{\langle k\rangle}$, with $\tau \in \{u_1, u_2, u_3, \vartheta_1, \vartheta_2, \vartheta_3\}$, represent the trial functions $\psi_i^{\langle k\rangle} = \psi_i^{\langle k\rangle}(\xi^{\langle k\rangle}, \eta^{\langle k\rangle})$ of the k-th plate, whereas the $(N_\tau + 1) \times 1$ column vectors $\boldsymbol{C}_\tau^{\langle k\rangle}$ contain the corresponding unknown Rayleigh-Ritz coefficients. To make these expressions more compact, Eqs. (20) are written in matrix form as

$$\boldsymbol{u}^{\langle k\rangle} = \begin{bmatrix} \boldsymbol{\Psi}_{u_1}^{\langle k\rangle} & \mathbf{0} & \mathbf{0} \\ \mathbf{0} & \boldsymbol{\Psi}_{u_2}^{\langle k\rangle} & \mathbf{0} \\ \mathbf{0} & \mathbf{0} & \boldsymbol{\Psi}_{u_3}^{\langle k\rangle} \end{bmatrix} \begin{Bmatrix} \boldsymbol{C}_{u_1}^{\langle k\rangle} \\ \boldsymbol{C}_{u_2}^{\langle k\rangle} \\ \boldsymbol{C}_{u_3}^{\langle k\rangle} \end{Bmatrix} = \begin{bmatrix} \boldsymbol{\Phi}_{u_1}^{\langle k\rangle} \\ \boldsymbol{\Phi}_{u_2}^{\langle k\rangle} \\ \boldsymbol{\Phi}_{u_3}^{\langle k\rangle} \end{bmatrix} \boldsymbol{U}^{\langle k\rangle} = \boldsymbol{\Phi}_u^{\langle k\rangle} \boldsymbol{U}^{\langle k\rangle} \tag{21a}$$

$$\boldsymbol{\vartheta} = \begin{bmatrix} \boldsymbol{\Psi}_{\vartheta_1}^{\langle k\rangle} & \mathbf{0} & \mathbf{0} \\ \mathbf{0} & \boldsymbol{\Psi}_{\vartheta_2}^{\langle k\rangle} & \mathbf{0} \\ \mathbf{0} & \mathbf{0} & \boldsymbol{\Psi}_{\vartheta_3}^{\langle k\rangle} \end{bmatrix} \begin{Bmatrix} \boldsymbol{C}_{\vartheta_1}^{\langle k\rangle} \\ \boldsymbol{C}_{\vartheta_2}^{\langle k\rangle} \\ \boldsymbol{C}_{\vartheta_3}^{\langle k\rangle} \end{Bmatrix} = \boldsymbol{\Phi}_\vartheta^{\langle k\rangle} \boldsymbol{\Theta}^{\langle k\rangle} \tag{21b}$$

The corresponding generalized strains are

$$\boldsymbol{\varepsilon}_0^{\langle k\rangle} = \boldsymbol{\mathcal{B}}_{pU}^{\langle k\rangle} \boldsymbol{U}^{\langle k\rangle} + \frac{1}{2} \boldsymbol{\mathcal{B}}_{nlU}^{\langle k\rangle} \boldsymbol{U}^{\langle k\rangle} + \bar{\boldsymbol{\mathcal{B}}}_{nlU}^{\langle k\rangle} \boldsymbol{U}^{\langle k\rangle} \tag{22a}$$

$$\boldsymbol{\kappa}^{\langle k\rangle} = \boldsymbol{\mathcal{B}}_{p\Theta}^{\langle k\rangle} \boldsymbol{\Theta}^{\langle k\rangle} \tag{22b}$$

$$\boldsymbol{\gamma}^{\langle k\rangle} = \boldsymbol{\mathcal{B}}_{nU}^{\langle k\rangle} \boldsymbol{U}^{\langle k\rangle} + \boldsymbol{\mathcal{B}}_{i\Theta}^{\langle k\rangle} \boldsymbol{\Theta}^{\langle k\rangle} \tag{22c}$$

where the discrete strain operators $\mathcal{B}$ are defined as

$$\mathcal{B}_{pU}^{\langle k\rangle} = \mathscr{D}_p \mathbf{\Phi}_u^{\langle k\rangle} \tag{23a}$$

$$\mathcal{B}_{p\vartheta}^{\langle k\rangle} = \mathscr{D}_p \mathbf{\Phi}_\vartheta^{\langle k\rangle} \tag{23b}$$

$$\mathcal{B}_{nlU}^{\langle k\rangle} = \left[\mathscr{D}_p \otimes \left(\mathbf{\Phi}_{u3}^{\langle k\rangle} \boldsymbol{U}^{\langle k\rangle}\right)\right] \mathscr{D}_n \mathbf{\Phi}_u^{\langle k\rangle} \tag{23c}$$

$$\bar{\mathcal{B}}_{nlU}^{\langle k\rangle} = \left[\mathscr{D}_p \otimes \bar{w}^{\langle k\rangle}\right] \mathscr{D}_n \mathbf{\Phi}_u^{\langle k\rangle} \tag{23d}$$

$$\mathcal{B}_{nU}^{\langle k\rangle} = \mathscr{D}_n \mathbf{\Phi}_u^{\langle k\rangle} \tag{23e}$$

$$\mathcal{B}_{i\Theta}^{\langle k\rangle} = \mathbf{\Phi}_\vartheta^{\langle k\rangle} \tag{23f}$$

3.2. Governing equations

Upon substitution of Eqs. (21) and (22) into Eq. (19), one obtains the discrete form of the functional Π whose first variation, after simple manipulations, gives

$$\begin{aligned}
\delta\Pi = \sum_{k=1}^{N_P} \int_{\Omega^{\langle k\rangle}} \Bigg\{ & \delta \boldsymbol{U}^{\langle k\rangle T} \Bigg[\left(\mathcal{B}_{pU}^{\langle k\rangle} + \mathcal{B}_{nlU}^{\langle k\rangle} + \bar{\mathcal{B}}_{nlU}^{\langle k\rangle}\right)^T \boldsymbol{A}_p^{\langle k\rangle} \left(\mathcal{B}_{pU}^{\langle k\rangle} + \frac{1}{2}\mathcal{B}_{nlU}^{\langle k\rangle} + \bar{\mathcal{B}}_{nlU}^{\langle k\rangle}\right) + \mathcal{B}_{nU}^{\langle k\rangle T} \boldsymbol{A}_n^{\langle k\rangle} \mathcal{B}_{nU}^{\langle k\rangle} \Bigg] \boldsymbol{U}^{\langle k\rangle} + \\
& \delta \boldsymbol{U}^{\langle k\rangle T} \Bigg[\left(\mathcal{B}_{pU}^{\langle k\rangle} + \mathcal{B}_{nlU}^{\langle k\rangle} + \bar{\mathcal{B}}_{nlU}^{\langle k\rangle}\right)^T \boldsymbol{B}^{\langle k\rangle} \mathcal{B}_{p\Theta}^{\langle k\rangle} + \mathcal{B}_{nU}^{\langle k\rangle T} \boldsymbol{A}_n^{\langle k\rangle} \mathcal{B}_{i\Theta}^{\langle k\rangle} \Bigg] \boldsymbol{\Theta}^{\langle k\rangle} + \\
& \delta \boldsymbol{\Theta}^{\langle k\rangle T} \Bigg[\mathcal{B}_{p\Theta}^{\langle k\rangle T} \boldsymbol{B}^{\langle k\rangle} \left(\mathcal{B}_{pU}^{\langle k\rangle} + \frac{1}{2}\mathcal{B}_{nlU}^{\langle k\rangle} + \bar{\mathcal{B}}_{nlU}^{\langle k\rangle}\right) + \mathcal{B}_{i\Theta}^{\langle k\rangle T} \boldsymbol{A}_n^{\langle k\rangle} \mathcal{B}_{nU}^{\langle k\rangle} \Bigg] \boldsymbol{U}^{\langle k\rangle} + \\
& \delta \boldsymbol{\Theta}^{\langle k\rangle T} \Bigg[\mathcal{B}_{p\Theta}^{\langle k\rangle T} \boldsymbol{D}^{\langle k\rangle} \mathcal{B}_{p\Theta}^{\langle k\rangle} + \mathcal{B}_{i\Theta}^{\langle k\rangle T} \boldsymbol{A}_n^{\langle k\rangle} \mathcal{B}_{i\Theta}^{\langle k\rangle} \Bigg] \boldsymbol{\Theta}^{\langle k\rangle} \Bigg\} d\Omega - \\
\sum_{k=1}^{N_P} \int_{\Omega^{\langle k\rangle}} & \left\{ \delta \boldsymbol{U}^{\langle k\rangle T} \left[\left(\mathcal{B}_{pU}^{\langle k\rangle} + \mathcal{B}_{nlU}^{\langle k\rangle} + \bar{\mathcal{B}}_{nlU}^{\langle k\rangle}\right)^T N_{\Delta T} + \mathbf{\Phi}_u^{\langle k\rangle T} \boldsymbol{q}^{\langle k\rangle} \right] + \delta \boldsymbol{\Theta}^{\langle k\rangle T} \left[\mathcal{B}_{p\Theta}^{\langle k\rangle T} M_{\Delta T} + \mathbf{\Phi}_\vartheta^{\langle k\rangle T} \boldsymbol{m}^{\langle k\rangle} \right] \right\} d\Omega - \\
\sum_{k=1}^{N_P} \int_{\partial\Omega_l^{\langle k\rangle}} & \left\{ \delta \boldsymbol{U}^{\langle k\rangle T} \mathbf{\Phi}_u^{\langle k\rangle T} \bar{\boldsymbol{N}}^{\langle k\rangle} + \delta \boldsymbol{\Theta}^{\langle k\rangle T} \mathbf{\Phi}_\vartheta^{\langle k\rangle T} \bar{\boldsymbol{M}}^{\langle k\rangle} \right\} d\partial\Omega - \\
\sum_{k=1}^{N_P} \int_{\partial\Omega_c^{\langle k\rangle}} & \Bigg\{ \delta \boldsymbol{U}^{\langle k\rangle T} \left[\mathbf{\Phi}_u^{\langle k\rangle T} \Xi_u^{\langle k\rangle T} \boldsymbol{\omega}_u^{\langle k\rangle} \Xi_u^{\langle k\rangle} \mathbf{\Phi}_u^{\langle k\rangle} \boldsymbol{U}^{\langle k\rangle} + \mathbf{\Phi}_u^{\langle k\rangle T} \Xi_u^{\langle k\rangle T} \boldsymbol{\omega}_u^{\langle k\rangle} \Xi_u^{\langle k\rangle} \bar{\boldsymbol{u}}^{\langle k\rangle} \right] + \\
& \delta \boldsymbol{\Theta}^{\langle k\rangle T} \left[\mathbf{\Phi}_\vartheta^{\langle k\rangle T} \Xi_\vartheta^{\langle k\rangle T} \boldsymbol{\omega}_\vartheta^{\langle k\rangle} \Xi_\vartheta^{\langle k\rangle} \mathbf{\Phi}_\vartheta^{\langle k\rangle} \boldsymbol{\Theta}^{\langle k\rangle} + \mathbf{\Phi}_\vartheta^{\langle k\rangle T} \Xi_\vartheta^{\langle k\rangle T} \boldsymbol{\omega}_\vartheta^{\langle k\rangle} \Xi_\vartheta^{\langle k\rangle} \bar{\boldsymbol{\vartheta}}^{\langle k\rangle} \right] \Bigg\} d\Omega + \\
\sum_{p=1}^{N_P-1} \sum_{q=p+1}^{N_P} \sum_{\alpha=p,q} \sum_{\beta=p,q} \int_{\Gamma_{pq}} & \Bigg\{ \delta \boldsymbol{U}^{\langle\alpha\rangle T} \mathbf{\Phi}_u^{\langle\alpha\rangle T} \boldsymbol{\Lambda}_u^{\langle\alpha\rangle T} \boldsymbol{\omega}_u^{\langle pq\rangle} \boldsymbol{\Lambda}_u^{\langle\beta\rangle} \mathbf{\Phi}_u^{\langle\beta\rangle} \boldsymbol{U}^{\langle\beta\rangle} + \\
& \delta \boldsymbol{\Theta}^{\langle\alpha\rangle T} \mathbf{\Phi}_\vartheta^{\langle\alpha\rangle T} \boldsymbol{\Lambda}_\vartheta^{\langle\alpha\rangle T} \boldsymbol{\omega}_\vartheta^{\langle pq\rangle} \boldsymbol{\Lambda}_\vartheta^{\langle\beta\rangle} \mathbf{\Phi}_\vartheta^{\langle\beta\rangle} \boldsymbol{\Theta}^{\langle\beta\rangle} \Bigg\} d\Gamma
\end{aligned} \tag{24}$$

It is worth noting that to obtain Eq. (24) the relation $\delta\left(\boldsymbol{\mathcal{B}}_{nlU}^{\langle k\rangle}\boldsymbol{U}^{\langle k\rangle}\right)=2\boldsymbol{\mathcal{B}}_{nlU}^{\langle k\rangle}\delta\boldsymbol{U}^{\langle k\rangle}$ is used.

Stationarity conditions, namely $\delta\Pi=0$, with respect to $\boldsymbol{U}^{\langle k\rangle}$ and $\boldsymbol{\Theta}^{\langle k\rangle}$ provide the system of nonlinear relations to be solved whose equations for $k=1,\ldots,N_P$ read as

$$\left\{\boldsymbol{K}_0^{\langle k\rangle}+\bar{\boldsymbol{K}}_0^{\langle k\rangle}+\boldsymbol{K}_1^{\langle k\rangle}+\bar{\boldsymbol{K}}_1^{\langle k\rangle}+\boldsymbol{K}_2^{\langle k\rangle}-\boldsymbol{K}_{\Delta T}^{\langle k\rangle}+\boldsymbol{R}^{\langle k\rangle}+\sum_{\substack{r=1\\r\neq k}}^{N_P}\left[\boldsymbol{P}_{kr}^{\langle k,k\rangle}\right]\right\}\boldsymbol{X}^{\langle k\rangle}-\sum_{\substack{r=1\\r\neq k}}^{N_P}\left[\boldsymbol{P}_{kr}^{\langle k,r\rangle}\right]\boldsymbol{X}^{\langle r\rangle}=\boldsymbol{F}_D^{\langle k\rangle}+\boldsymbol{F}_L^{\langle k\rangle}+\boldsymbol{F}_{\Delta T}^{\langle k\rangle} \tag{25}$$

where the vectors ${\boldsymbol{X}^{\langle k\rangle}}^T=\left\{{\boldsymbol{U}^{\langle k\rangle}}^T\ {\boldsymbol{\Theta}^{\langle k\rangle}}^T\right\}$ are introduced and

$$\boldsymbol{K}_0^{\langle k\rangle}=\int_{\Omega^{\langle k\rangle}}\begin{bmatrix}{\boldsymbol{\mathcal{B}}_{pU}^{\langle k\rangle}}^T\boldsymbol{A}_p^{\langle k\rangle}\boldsymbol{\mathcal{B}}_{pU}^{\langle k\rangle}+{\boldsymbol{\mathcal{B}}_{nU}^{\langle k\rangle}}^T\boldsymbol{A}_n^{\langle k\rangle}\boldsymbol{\mathcal{B}}_{nU}^{\langle k\rangle} & {\boldsymbol{\mathcal{B}}_{pU}^{\langle k\rangle}}^T\boldsymbol{B}^{\langle k\rangle}\boldsymbol{\mathcal{B}}_{p\Theta}^{\langle k\rangle}+{\boldsymbol{\mathcal{B}}_{nU}^{\langle k\rangle}}^T\boldsymbol{A}_n^{\langle k\rangle}\boldsymbol{\mathcal{B}}_{i\Theta}^{\langle k\rangle}\\ {\boldsymbol{\mathcal{B}}_{p\Theta}^{\langle k\rangle}}^T\boldsymbol{B}^{\langle k\rangle}\boldsymbol{\mathcal{B}}_{pU}^{\langle k\rangle}+{\boldsymbol{\mathcal{B}}_{i\Theta}^{\langle k\rangle}}^T\boldsymbol{A}_n^{\langle k\rangle}\boldsymbol{\mathcal{B}}_{nU}^{\langle k\rangle} & {\boldsymbol{\mathcal{B}}_{p\Theta}^{\langle k\rangle}}^T\boldsymbol{D}^{\langle k\rangle}\boldsymbol{\mathcal{B}}_{p\Theta}^{\langle k\rangle}+{\boldsymbol{\mathcal{B}}_{i\Theta}^{\langle k\rangle}}^T\boldsymbol{A}_n^{\langle k\rangle}\boldsymbol{\mathcal{B}}_{i\Theta}^{\langle k\rangle}\end{bmatrix}d\Omega \tag{26a}$$

$$\boldsymbol{K}_1^{\langle k\rangle}=\int_{\Omega^{\langle k\rangle}}\begin{bmatrix}\frac{1}{2}{\boldsymbol{\mathcal{B}}_{pU}^{\langle k\rangle}}^T\boldsymbol{A}_p^{\langle k\rangle}\boldsymbol{\mathcal{B}}_{nlU}^{\langle k\rangle}+{\boldsymbol{\mathcal{B}}_{nlU}^{\langle k\rangle}}^T\boldsymbol{A}_p^{\langle k\rangle}\boldsymbol{\mathcal{B}}_{pU}^{\langle k\rangle} & {\boldsymbol{\mathcal{B}}_{nlU}^{\langle k\rangle}}^T\boldsymbol{B}^{\langle k\rangle}\boldsymbol{\mathcal{B}}_{p\Theta}^{\langle k\rangle}\\ \frac{1}{2}{\boldsymbol{\mathcal{B}}_{p\Theta}^{\langle k\rangle}}^T\boldsymbol{B}^{\langle k\rangle}\boldsymbol{\mathcal{B}}_{nlU}^{\langle k\rangle} & \boldsymbol{0}\end{bmatrix}d\Omega \tag{26b}$$

$$\boldsymbol{K}_2^{\langle k\rangle}=\int_{\Omega^{\langle k\rangle}}\begin{bmatrix}\frac{1}{2}{\boldsymbol{\mathcal{B}}_{nlU}^{\langle k\rangle}}^T\boldsymbol{A}_p^{\langle k\rangle}\boldsymbol{\mathcal{B}}_{nlU}^{\langle k\rangle} & \boldsymbol{0}\\ \boldsymbol{0} & \boldsymbol{0}\end{bmatrix}d\Omega \tag{26c}$$

$$\boldsymbol{K}_{\Delta T}^{\langle k\rangle}=\int_{\Omega}\begin{bmatrix}{\boldsymbol{\mathcal{B}}_{nU}^{\langle k\rangle}}^T\widehat{\boldsymbol{N}}_{\Delta T}^{\langle k\rangle}\boldsymbol{\mathcal{B}}_{nU}^{\langle k\rangle} & \boldsymbol{0}\\ \boldsymbol{0} & \boldsymbol{0}\end{bmatrix}d\Omega \tag{26d}$$

$$\bar{\boldsymbol{K}}_0^{\langle k\rangle}=\int_{\Omega^{\langle k\rangle}}\begin{bmatrix}{\boldsymbol{\mathcal{B}}_{pU}^{\langle k\rangle}}^T\boldsymbol{A}_p^{\langle k\rangle}\bar{\boldsymbol{\mathcal{B}}}_{nlU}^{\langle k\rangle}+{\bar{\boldsymbol{\mathcal{B}}}_{nlU}^{\langle k\rangle}}^T\boldsymbol{A}_p^{\langle k\rangle}\boldsymbol{\mathcal{B}}_{pU}^{\langle k\rangle}+{\bar{\boldsymbol{\mathcal{B}}}_{nlU}^{\langle k\rangle}}^T\boldsymbol{A}_p^{\langle k\rangle}\bar{\boldsymbol{\mathcal{B}}}_{nlU}^{\langle k\rangle} & {\bar{\boldsymbol{\mathcal{B}}}_{nlU}^{\langle k\rangle}}^T\boldsymbol{B}^{\langle k\rangle}\boldsymbol{\mathcal{B}}_{p\Theta}^{\langle k\rangle}\\ {\boldsymbol{\mathcal{B}}_{p\Theta}^{\langle k\rangle}}^T\boldsymbol{B}^{\langle k\rangle}\bar{\boldsymbol{\mathcal{B}}}_{nlU}^{\langle k\rangle} & \boldsymbol{0}\end{bmatrix}d\Omega \tag{26e}$$

$$\bar{\boldsymbol{K}}_1^{\langle k\rangle}=\int_{\Omega^{\langle k\rangle}}\begin{bmatrix}{\boldsymbol{\mathcal{B}}_{nlU}^{\langle k\rangle}}^T\boldsymbol{A}_p^{\langle k\rangle}\bar{\boldsymbol{\mathcal{B}}}_{nlU}^{\langle k\rangle}+\frac{1}{2}{\bar{\boldsymbol{\mathcal{B}}}_{nlU}^{\langle k\rangle}}^T\boldsymbol{A}_p^{\langle k\rangle}\boldsymbol{\mathcal{B}}_{nlU}^{\langle k\rangle} & \boldsymbol{0}\\ \boldsymbol{0} & \boldsymbol{0}\end{bmatrix}d\Omega \tag{26f}$$

$$\boldsymbol{P}_{pq}^{\langle r,s\rangle}=\int_{\Gamma_{pq}}\begin{bmatrix}{\boldsymbol{\Phi}_u^{\langle r\rangle}}^T{\boldsymbol{\Lambda}_u^{\langle r\rangle}}^T\boldsymbol{\omega}_u^{\langle pq\rangle}\boldsymbol{\Lambda}_u^{\langle s\rangle}\boldsymbol{\Phi}_u^{\langle s\rangle} & \boldsymbol{0}\\ \boldsymbol{0} & {\boldsymbol{\Phi}_\vartheta^{\langle r\rangle}}^T{\boldsymbol{\Lambda}_\vartheta^{\langle r\rangle}}^T\boldsymbol{\omega}_\vartheta^{\langle pq\rangle}\boldsymbol{\Lambda}_\vartheta^{\langle s\rangle}\boldsymbol{\Phi}_\vartheta^{\langle s\rangle}\end{bmatrix}d\Gamma \tag{26g}$$

$$\boldsymbol{R}^{\langle k\rangle} = \int_{\partial\Omega_c^{\langle k\rangle}} \begin{bmatrix} \boldsymbol{\Phi}_u^{\langle k\rangle\,T} \boldsymbol{\Xi}_u^{\langle k\rangle\,T} \boldsymbol{\omega}_u^{\langle k\rangle}\, \boldsymbol{\Xi}_u^{\langle k\rangle} \boldsymbol{\Phi}_u^{\langle k\rangle} & \mathbf{0} \\ \mathbf{0} & \boldsymbol{\Phi}_\vartheta^{\langle k\rangle\,T} \boldsymbol{\Xi}_\vartheta^{\langle k\rangle\,T} \boldsymbol{\omega}_\vartheta^{\langle k\rangle}\, \boldsymbol{\Xi}_\vartheta^{\langle k\rangle} \boldsymbol{\Phi}_\vartheta^{\langle k\rangle} \end{bmatrix} d\partial\Omega \tag{26h}$$

$$\boldsymbol{F}_D^{\langle k\rangle} = \begin{Bmatrix} \int_\Omega \boldsymbol{\Phi}_u^{\langle k\rangle\,T} \boldsymbol{q}^{\langle k\rangle} d\Omega \\ \int_\Omega \boldsymbol{\Phi}_\vartheta^{\langle k\rangle\,T} \boldsymbol{m}^{\langle k\rangle} d\Omega \end{Bmatrix} \tag{26i}$$

$$\boldsymbol{F}_L^{\langle k\rangle} = \begin{Bmatrix} \int_{\partial\Omega_c} \left[\boldsymbol{\Phi}_u^{\langle k\rangle\,T} \widehat{\boldsymbol{\Xi}}_u^{\langle k\rangle}\, \bar{\boldsymbol{u}}^{\langle k\rangle}\right] d\partial\Omega + \int_{\partial\Omega_l} \boldsymbol{\Phi}_u^{\langle k\rangle\,T} \bar{\boldsymbol{N}}^{\langle k\rangle} d\partial\Omega \\ \int_{\partial\Omega_c} \left[\boldsymbol{\Phi}_\vartheta^{\langle k\rangle\,T} \widehat{\boldsymbol{\Xi}}_\vartheta^{\langle k\rangle}\, \bar{\boldsymbol{\vartheta}}^{\langle k\rangle}\right] d\partial\Omega + \int_{\partial\Omega_l} \boldsymbol{\Phi}_\vartheta^{\langle k\rangle\,T} \bar{\boldsymbol{M}}^{\langle k\rangle} d\partial\Omega \end{Bmatrix} \tag{26j}$$

$$\boldsymbol{F}_{\Delta T}^{\langle k\rangle} = \begin{Bmatrix} \int_\Omega \left[\left(\boldsymbol{\mathcal{B}}_{pU}^{\langle k\rangle} + \bar{\boldsymbol{\mathcal{B}}}_{nlU}^{\langle k\rangle}\right)^T N_{\Delta T}^{\langle k\rangle}\right] d\Omega \\ \int_\Omega \left[\boldsymbol{\mathcal{B}}_{p\Theta}^{\langle k\rangle\,T} M_{\Delta T}^{\langle k\rangle}\right] d\Omega \end{Bmatrix} \tag{26k}$$

Note, that the matrices $\boldsymbol{K}_2^{\langle k\rangle}$, $\boldsymbol{K}_1^{\langle k\rangle}$ and $\bar{\boldsymbol{K}}_1^{\langle k\rangle}$ depend on the unknown vectors $\boldsymbol{X}^{\langle k\rangle}$. The matrix $\boldsymbol{K}_{\Delta T}^{\langle k\rangle}$ is the stiffness matrix associated with the thermal membrane stress distribution and it is obtained by considering that

$$\boldsymbol{\mathcal{B}}_{nlU}^{\langle k\rangle\,T} \boldsymbol{N}_{\Delta T}^{\langle k\rangle} = \left(\left[\boldsymbol{\mathscr{D}}_p \otimes \left(\boldsymbol{\Phi}_{u_3}^{\langle k\rangle} \boldsymbol{U}^{\langle k\rangle}\right)\right] \boldsymbol{\mathscr{D}}_n \boldsymbol{\Phi}_u^{\langle k\rangle}\right)^T \boldsymbol{N}_{\Delta T}^{\langle k\rangle} = \boldsymbol{\mathcal{B}}_{nU}^{\langle k\rangle\,T} \widehat{\boldsymbol{N}}_{\Delta T}^{\langle k\rangle} \boldsymbol{\mathcal{B}}_{nU}^{\langle k\rangle} \boldsymbol{U}^{\langle k\rangle} \tag{27}$$

where

$$\widehat{\boldsymbol{N}}_{\Delta T}^{\langle k\rangle} = \begin{bmatrix} N_{1_{\Delta T}}^{\langle k\rangle} & N_{3_{\Delta T}}^{\langle k\rangle} & 0 \\ N_{3_{\Delta T}}^{\langle k\rangle} & N_{2_{\Delta T}}^{\langle k\rangle} & 0 \\ 0 & 0 & 0 \end{bmatrix} \tag{28}$$

Note, by using the penalty method to enforce natural boundary conditions and continuity at common edges of adjacent domains the dimension of the stiffness operator remains unchanged. In fact, only the sparsity of the resulting stiffness matrix reduces due to the presence of off-diagonal terms. Furthermore, properties including symmetry and positive-definiteness remain.

3.3. Solution of the Governing equations

A Newton-Raphson incremental-iterative solution procedure is implemented, where at a given solution step, for ith iteration, Eq. (25) can be written as

$$\left\{\left[\boldsymbol{K}_{1t}^{\langle k\rangle}+\bar{\boldsymbol{K}}_{1t}^{\langle k\rangle}+\boldsymbol{K}_{2t}^{\langle k\rangle}+\boldsymbol{K}_{G}^{\langle k\rangle}-\boldsymbol{K}_{\Delta T}^{\langle k\rangle}\right]\Big|_{i}+\boldsymbol{K}_{0}^{\langle k\rangle}+\boldsymbol{R}^{\langle k\rangle}+\sum_{\substack{r=1\\r\neq k}}^{N_P}\boldsymbol{P}_{kk}^{\langle k,r\rangle}\right\}\boldsymbol{\Delta X}_{i+1}^{\langle k\rangle}-\sum_{\substack{r=1\\r\neq k}}^{N_P}\boldsymbol{P}_{kr}^{\langle k,r\rangle}\boldsymbol{\Delta X}_{i+1}^{\langle r\rangle}=-\boldsymbol{\Delta\mathcal{R}}_{i}\left(\boldsymbol{\delta X}_{i}^{\langle k\rangle},\boldsymbol{\delta X}_{i}^{\langle r\rangle}\right) \tag{29}$$

being $\boldsymbol{\delta X}$ the known solution of the previous iteration. The imbalance force vector $\boldsymbol{\Delta\mathcal{R}}_i$ and the incremental vector of the system unknowns $\boldsymbol{\Delta X}_{i+1}^{\langle j\rangle}$ are given by

$$\begin{aligned}\boldsymbol{\Delta\mathcal{R}}_{i}=&\left\{\boldsymbol{K}_{0}^{\langle k\rangle}+\bar{\boldsymbol{K}}_{0}^{\langle k\rangle}+\boldsymbol{K}_{1}^{\langle k\rangle}+\bar{\boldsymbol{K}}_{1}^{\langle k\rangle}+\boldsymbol{K}_{2}^{\langle k\rangle}-\boldsymbol{K}_{\Delta T}^{\langle k\rangle}+\boldsymbol{R}^{\langle k\rangle}+\sum_{\substack{r=1\\r\neq k}}^{N_P}\left[\boldsymbol{P}_{kr}^{\langle k,k\rangle}\right]\right\}\delta\boldsymbol{X}_{i}^{\langle k\rangle}\\&-\sum_{\substack{r=1\\r\neq k}}^{N_P}\left[\boldsymbol{P}_{kr}^{\langle k,r\rangle}\right]\delta\boldsymbol{X}_{i}^{\langle r\rangle}-\boldsymbol{F}_{D}^{\langle k\rangle}-\boldsymbol{F}_{L}^{\langle k\rangle}-\boldsymbol{F}_{\Delta T}^{\langle k\rangle}\end{aligned} \tag{30}$$

$$\boldsymbol{\Delta X}_{i+1}^{\langle j\rangle}=\boldsymbol{X}_{i+1}^{\langle j\rangle}-\delta\boldsymbol{X}_{i}^{\langle j\rangle} \tag{31}$$

The matrices $\boldsymbol{K}_{1t}^{\langle k\rangle}$ and $\boldsymbol{K}_{2t}^{\langle k\rangle}$ are the linear and the nonlinear terms of the tangent stiffness matrix, while the matrices $\bar{\boldsymbol{K}}_{1t}^{\langle k\rangle}$ and $\boldsymbol{K}_{G}^{\langle k\rangle}$ are the linear term of the tangent stiffness matrix due to the initial imperfection and the geometric stiffness matrix, respectively. Their expressions can be obtained by differentiating Eq. (25) and are given in Appendix A. Solving the linearized system, namely Eq.(29), for $\boldsymbol{\Delta X}_{i+1}^{\langle j\rangle}$, the incremental system's unknown vectors are updated as

$$\boldsymbol{X}_{i+1}^{\langle j\rangle}=\delta\boldsymbol{X}_{i}^{\langle j\rangle}+\boldsymbol{\Delta X}_{i+1}^{\langle j\rangle} \tag{32}$$

The iterative procedure is stopped and the incremental vectors are considered as converged when the normalized $\mathcal{L}^2$-norm of the system's unknown incremental vector $\|\boldsymbol{\Delta X}_{i+1}\|/\|\boldsymbol{X}_{i+1}\|$ is less than a prescribed value.

3.4. Linearized buckling analysis

Despite the present paper being focused on the postbuckling behaviour of VAT stiffened plates, for the sake of completeness, the system for linearized buckling analysis is presented. Indeed, the linearized buckling eigenvalue problem can be straightforwardly deduced from Eq. (29) [47, 50] and, for $k = 1, \ldots, N_P$, is written as

$$\left\{ \boldsymbol{K}_0^{\langle k \rangle} + \boldsymbol{R}^{\langle k \rangle} + \sum_{\substack{r=1 \\ r \neq k}}^{N_P} \boldsymbol{P}_{kk}^{\langle k,r \rangle} + \lambda \boldsymbol{K}_G^{\langle k \rangle} \right\} \boldsymbol{X}^{\langle k \rangle} - \sum_{\substack{r=1 \\ r \neq k}}^{N_P} \boldsymbol{P}_{kr}^{\langle k,r \rangle} \boldsymbol{X}^{\langle r \rangle} = \boldsymbol{0} \tag{33}$$

where the eigenvalue λ is the load multiplier and the eigenvectors $\boldsymbol{X}^{\langle k \rangle}$ are the Rayleigh-Ritz coefficients associated with the buckling mode. In Eq. (33), the matrix $\boldsymbol{K}_G$ is computed with the membrane stress distribution $\widehat{\boldsymbol{N}}^{\langle k \rangle}$ corresponding to the pre-buckled state. The evaluation of pre-buckled membrane stress distribution deserves particular attention especially when non-symmetric and/or VAT laminates are analyzed. Actually, during the pre-buckling regime, significant in-plane load redistribution triggered by the transverse displacement can occur and, for an accurate estimation of buckling, the nonlinear problem which couple the transverse displacements and the in-plane loads should be solved [51].

4. Implementation

A computer code has been developed for the proposed Rayleigh-Ritz solution procedure with the following implementation characteristics.

The trial functions $\psi_i(\xi, \eta)$ use orthogonal polynomials, which prove to be accurate and efficient for plate problems [52]. In particular, the trial functions are defined as

$$\psi_{(nM+m)} = \varphi_n(\xi)\, \chi_m(\eta) \qquad n = 0, ..., N; \quad m = 0, ..., M \tag{34}$$

where M and N are the order of the approximated variable expansion along

the ξ and η coordinates, and $\varphi_n(\xi)$ and $\chi_m(\eta)$ are one dimensional Legendre orthogonal polynomials

$$\varphi_n(\zeta) = \chi_n(\zeta) = \frac{1}{2^n n!}\frac{d^n}{d\zeta^n}\left[\left(\zeta^2-1\right)^n\right] \tag{35}$$

These trial functions, in general, do not satisfy the essential boundary conditions which are imposed as a constraint by the variational statement (see Eq. (19)).

The penalty coefficients are associated with artificial springs distributed along the joined edges between plates [53]. Those stiffnesses per unit length are set as 10^S-times the mean of a representative stiffness coefficient of the involved contiguous plates. For the translational springs the representative stiffness coefficient is chosen as the maximum Young's modulus of the laminate, whereas for the rotational springs it is chosen as the maximum value of the laminate's Young's modulus times the square of the plate thickness. Sensitivity analyses led to a value of $S = 5$ being chosen so that no appreciable variations in the results was observed for S in the range from 3 to 7 [43, 53].

Assuming a uniform reference temperature T_{ref} for the whole assembled structure, the temperature increment for the k-th plate is expressed as

$$\Delta T^{\langle k\rangle} = T_0^{\langle k\rangle} + \left(x_3^{\langle k\rangle} + \bar{x}_3^{\langle k\rangle}\right) T_1^{\langle k\rangle} \tag{36}$$

where $T_0^{\langle k\rangle} = T_0^{\langle k\rangle}(x_1, x_2)$ is the temperature increment of the modelling plane and $T_1^{\langle k\rangle} = T_1^{\langle k\rangle}(x_1, x_2)$ is its variation across the plate thickness. The condition (36) can be expressed in terms of the temperature distributions $T_t^{\langle k\rangle}$ and $T_b^{\langle k\rangle}$ of the plate's top and bottom surface as

$$\begin{aligned}\Delta T^{\langle k\rangle} =& T_0^{\langle k\rangle} + \left(x_3^{\langle k\rangle} + \bar{x}_3^{\langle k\rangle}\right) T_1^{\langle k\rangle} \\ =& \frac{1}{2}\left(\Delta T_t^{\langle k\rangle} + \Delta T_b^{\langle k\rangle}\right) + \left(x_3^{\langle k\rangle} + \bar{x}_3^{\langle k\rangle}\right)\frac{T_t^{\langle k\rangle} - T_b^{\langle k\rangle}}{t_h^{\langle k\rangle}}\end{aligned} \tag{37}$$

where $t_h^{\langle k\rangle}$ is the plate thickness and $\Delta T_t^{\langle k\rangle}$, $\Delta T_b^{\langle k\rangle}$ are the temperature increments of the top and bottom surface respectively. In order to consider at most

a bilinear distribution of the temperatures over the top and bottom surfaces, T_t and T_b are expressed as

$$T_t^{\langle k\rangle}\left(\xi^{\langle k\rangle},\eta^{\langle k\rangle}\right)=\sum_{\alpha=1}^{4} g_\alpha(\xi^{\langle k\rangle},\eta^{\langle k\rangle})\,T_{t_\alpha}^{\langle k\rangle} \tag{38a}$$

$$T_b^{\langle k\rangle}\left(\xi^{\langle k\rangle},\eta^{\langle k\rangle}\right)=\sum_{\alpha=1}^{4} g_\alpha(\xi^{\langle k\rangle},\eta^{\langle k\rangle})\,T_{b_\alpha}^{\langle k\rangle} \tag{38b}$$

where g_α are the quadrilateral shape functions defined in Eqs. (2) and $T_{t_\alpha}^{\langle k\rangle}$, $T_{b_\alpha}^{\langle k\rangle}$ are the top and bottom surface temperatures evaluated at the α-th vertex of the plate.

The system matrices, Eqs. (26) and (A.7), are numerically computed by Legendre-Gauss quadrature formulas. Their evaluation requires the description of the plate constitutive law that for VAT laminates depends on the in-plane coordinates through the variation of the fibre orientation θ that is assumed to be

$$\theta^{\langle k\rangle}(x_1^{\langle k\rangle},x_2^{\langle k\rangle})=\theta^{\langle k\rangle}(\xi^{\langle k\rangle},\eta^{\langle k\rangle})={\theta_0}^{\langle k\rangle}+\sum_{i=0}^{M}\psi_i^{\langle k\rangle}C_{\theta_i}^{\langle k\rangle} \tag{39}$$

where $\theta_0^{\langle k\rangle}$ is a constant fibres pattern angle. Considering the possible complexity of fibres orientation in thin-walled structures, to simplify the data preparation, the fibre orientation angle variation of each plate of the structure is referred to the vector $\hat{\boldsymbol{n}}_0^{\langle k\rangle}$, which lies on the modelling plane and defines the zero fibre orientation. The unknown coefficients C_{θ_i} are determined by collocation of Eq. (39) at a set of $(M+1)$ reference points in the plate domain where the fibre angles are given as input data. In the current implementation of the computer code, linear variation ($M=1$) of fibre orientation angles is considered although more general distribution can be straightforwardly considered.

In particular, fibre angle variations as introduced in Ref. [2] are considered. Hence, referring to Fig.1, let us consider an arbitrary reference point A to be the origin of the axis r, which is rotated by an angle θ_0 from the zero fibre angle direction vector $\hat{\boldsymbol{n}}_0$, θ'_A be the the angle between the fibre and the direction r

at the point A. Moving along the r-axis, at a characteristic distance d from the point A, the fibre angle becomes θ'_B at the point B. The fibre angle along the r-axis is assumed to vary as

$$\theta(r) = \theta_0 + (\theta'_B - \theta'_A)\frac{\tilde{r}}{d} + \theta'_A \tag{40}$$

where $\tilde{r}$ can be specified as $\tilde{r} = r$ or $\tilde{r} = |r|$. It is worth noting that these definitions allow both symmetric and unsymmetric variations of the fibres angle to be described with respect to the chosen starting point. Eq. (40) defines the fibre angles on the r-axis; it is assumed that the fibre orientation at other points in the domain is obtained by shifting this basic path in a direction perpendicular to the r-axis. Thus the fibre orientation becomes a function of both local in-plane coordinates, namely $\theta = \theta(x_1, x_2)$. According to this kind of fibre pattern, a VAT ply is described by the notation $\theta_0\langle\theta'_A|\theta'_B\rangle$ if $\tilde{r} = |r|$ or $\theta_0\langle\langle\theta'_A|\theta'_B\rangle\rangle$ if $\tilde{r} = r$. The laminate layup is then described by the conventional representation assuming also that a $\pm$ sign in front of either θ_0 or $\langle\theta'_A|\theta'_B\rangle$ or $\langle\langle\theta'_A|\theta'_B\rangle\rangle$ means that there are two adjacent layers with equal and opposite variation of the fibre angle. This notation actually extends that introduced in Ref. [2].

Offsets $\bar{x}_3^{\langle k\rangle}$ are used to choose the physical meaning of the generalized variables and also ensure the application of continuity requirements is consistent, namely Eqs. (17), along the edges of contiguous plates with different thickness and stacking sequences.

Finally, the system of equations is solved by the Newton-Raphson solution scheme, stopping the iterative procedure when the normalized $\mathcal{L}^2$-norm of the system unknowns' incremental vector $\|\boldsymbol{\Delta X}_{i+1}\|/\|\boldsymbol{X}_{i+1}\|$ is less than 10^{-6}. Furthermore, a step-size control procedure is implemented that allows for the reduction of the step size if the convergence criteria of the solution fails during the iteration procedure.

5. Applications and results

The proposed formulation and the developed analysis tool allows for the analysis of panels exhibiting general stacking sequences and subjected to different domain loads, membrane boundary loads, moments, prescribed displacements and thermal loading conditions. Linear buckling analyses and nonlinear postbuckling analyses have been carried out successfully for different configurations. In this section some representative results are presented to show the potential of the approach, focusing on the postbuckling behaviour of VAT stiffened panels undergoing both mechanical and thermal loadings.

The presented results follow convergence analyses carried out by varying the polynomial order for the variables approximation. The results of these convergence analyses show trends similar to those discussed in Ref. [52] and they are not reported here for the sake of conciseness.

First, square VAT flat plates, with edge lengths $a = 1.0\,m$ are analysed. Let the global reference system be chosen with the X_1 and X_2 axes parallel to the panel edges and with the origin at the plate centre. Plies with a linear variation of the fibre angle along the X_1 direction are considered, assuming that the characteristic length d defined in Eq. (40) starts from the edge midpoint and equals the plate half-width. Four different test cases are considered, namely $TC1$, $TC2$, $TC3$ and $TC4$, all using balanced symmetric layups, with 12 constant thickness plies, each $0.1272\,mm$ thick. The considered layup is $[0 \pm \langle 45|0\rangle]_{3_S}$ for test cases $TC1$, $TC3$, and $[45 \pm \langle 90|0\rangle]_{3_S}$ for test cases $TC2$ and $TC4$. The material properties for the orthotropic layers are set as

$$\begin{aligned} &E_1 = 181.0\,GPa; \quad E_2 = 10.27\,GPa; \quad G_{12} = 7.17\,GPa; \\ &\nu_{12} = 0.28; \quad \alpha_1 = -0.11\,\mu\varepsilon/K; \quad \alpha_2 = 25.2\,\mu\varepsilon/K; \end{aligned} \tag{41}$$

Referring to the test case $TC1$, the plate undergoes uniaxial compression along the X_1 direction and a clamped boundary condition is assumed with free in-plane displacements along all the edges. With reference to the test case $TC2$, the plate undergoes biaxial compression, assuming a clamped condition along

the edges parallel to the X_1 axis and a simply supported condition along the edges of the plate parallel to the X_2 axis. Also in this case the in-plane displacements are assumed to be free along all of the plate's edges. Referring to the test cases $TC3$ and $TC4$, the plates undergoes a uniform change in temperature. For both the test cases $TC3$ and $TC4$ the in-plane displacements are assumed to be clamped along all of the plate's edges, while the same boundary conditions of $TC1$ and $TC2$ respectively are considered. For all of the proposed test cases, a small imperfection of the panel is introduced as a bisinusoidal prescribed deflection of the plate midplane with amplitude equal to the 0.1% of the plate thickness. Furthermore, all analyses are conducted with a load-control solution procedure. With the aim of validating the subdomain decomposition technique, even if not necessary for this example, the analyses have been performed by modelling the panels with four square plates and assuming the same order of polynomial approximation, for all variables; the following results refer to the approximation scheme with $N = M = 6$ which gives a total of 864 DOFs. Note that the chosen VAT layups do not represent optimized layups for the chosen load-cases, rather serve to demonstrate the robustness and wide applicability of the modelling approach. The results obtained for the postbuckling of the $TC1$ and $TC2$ panels are compared with those obtained by Madeo et al. [54] and with finite element analysis results. For test cases $TC3$ and $TC4$ the presented results are compared only with finite elements as, to the best of the authors' knowledge, no literature results are available for the postbuckling of VAT plates undergoing thermal loading conditions. Finite element analyses were performed with Abaqus, using $S4R$ shell elements. To model the fibre angle distributions, a subroutine was implemented to generate meshes where each element has an independent constant fibre orientation. Meshes with 8100 square elements and 90 different layups, for a total of 47526 DOFs, were used as they provided converged results. Figs. 2 and 3 show the obtained results in terms of transverse displacement of the plate's centre versus the applied load. The transverse displacement is normalised with respect to the plate thickness, while the applied load is normalised with respect to the corresponding critical buckling value. As

regards accuracy, excellent agreement between the present results and finite element analysis is observed for all of the investigated test cases; good agreement with Ref. [54] is also observed for test cases $TC1$ and $TC2$. Only regarding $TC1$ test case, a slightly worse match with results obtained by Ref. [54] is observed for large displacements. Figs. 4 and 5 show the obtained results for the test cases $TC3$ and $TC4$ respectively, in terms of the transverse displacement of the plates' centre versus the applied change in temperature. The transverse displacement is normalised with respect to the plate thickness, while the applied thermal load is normalised with respect to the corresponding critical buckling value. Also for these test cases, excellent agreement between the present results and finite element analysis is observed, with only a slightly difference for large displacements of the $TC3$ test case.

The postbuckling behaviour of a blade stiffened composite VAT plate is now investigated. The chosen panel geometry is based on Nagendra et al. [55, 56] and it is depicted in Fig.6. In order to show the generality of the proposed approach, for the skin and the stringer's flange an antisymmetric layup is chosen. For these elements a linear variation of the fibre angle is assumed along the X_1-axis with the VAT characteristic lengths starting from the edge midpoint to the plate's half-width, that is $a/2$ and $a_s/2$, respectively. For the stringer web a symmetric layup is chosen with the fibre angle varying along the X_3-axis and the VAT characteristic length starting from the edge top end to the plate's width, namely h. The VAT layups for the skin, the stringer flange and the stringer web are listed in Table 1. The layups consist of $0.25\,mm$ thick orthotropic plies whose material properties are shown in Table 2.

Symmetry restraints are imposed on the two lateral sides of the panel and a simply supported condition is considered on both the front and rear edges. The chosen panel geometry and the considered boundary conditions allows for its configuration to be considered as a representative section of a wide wing cover supported between spars and adjacent ribs [57], and is useful to investigate for local buckling phenomena [41]. With reference to the loading conditions, the panel undergoes a uniaxial compression displacement $\Delta_2 = 0.5\,mm$ along the

X_2-axis which is applied on both the front and rear edges. Furthermore a uniform thermal load $\Delta T = 120°K$ is imposed over the skin and the stiffener. A small imperfection of the panel is introduced as a bisinusoidal prescribed deflection of the skin midplane with amplitude equal to the 0.1% of the skin thickness. Then, the analysis is conducted with a displacement-control solution procedure. A domain decomposition consisting of five plates with appropriate layup is considered, namely one plate for each part of the skin outside the stringer flange, two plates joined along the web line for the stringer feet and one plate for the stiffener web. The same order of polynomial approximation for the variables is assumed for all plates and the following results refer to the approximation scheme with $N = M = 8$ and 2430 DOFs, which provided converged results. Finite element analysis has been performed with Abaqus, using mesh with 32120 $S4R$ elements and 146 different layups, for a total of 194910 DOFs, which also provided converged results. Fig. 7 shows the results in terms of transverse displacement u_3 of the two points of the panel (A) and (B) as shown in Fig. 6 versus the applied load factor. The transverse displacement is normalised with respect to the panel's skin thickness, while the applied load factor is normalised with respect to the corresponding critical buckling value. The postbuckling equilibrium paths in Fig.7 give excellent agreement with finite element results. As expected, the antisymmetric layup of the skin as well as the unsymmetric distribution of the plate's thicknesses triggers appreciable transverse displacements of the panel upon initial loadings. The buckled panel deformation corresponding to the maximum applied load is depicted in Fig.8; the deformation of panel is characterized by a single half wave involving both the skin and the stiffener web. These results, presented as representative also of other analyses carried out, show the accuracy of the proposed approach and its capacity to model composite VAT stiffened plates in the postbuckling regime. The analyses show that the method can provide the same accuracy level as finite elements with a remarkable reduced number of unknowns. It is worth nothing that the proposed approach also simplifies the data preparation as the introduced domain decomposition actually relates to geometrical modelling and not

to a mesh-like support for the approximation of variables.

Finally, to illustrate the potential of the method in modelling complex problems, the result for the postbuckling solution of a composite VAT wingbox structure is presented. This is a challenging case to analyze, which is representative of typical aerospace structures problems and whose results are considered able to show the capability of the proposed solution to analyze complex VAT structures. The chosen wingbox section geometry is typical of a medium-range flight aircraft and also include stiffeners runout as depicted in Fig.9. In order to show the generality of the proposed approach, both straight fibre and variable angle tow laminates are considered. Namely, straight fibre laminates are considered for the lateral panels of the wingbox and for the webs of T-stiffeners. For these elements the lamination angle is defined with respect to the X_3-axis. Straight fibre laminates are also considered for the angle stiffeners at the wingbox's corners, where the lamination angle is defined with respect to the X_1-axis and the X_3-axis for the horizontal and the vertical flange, respectively. For the upper and lower skin and for the T-stringer's flange a VAT symmetric layup is chosen. Referring to Fig.10, for these elements a linear variation of the fibre angle is assumed along the X_1-axis with the VAT characteristic lengths starting from the edge midpoint to the plate's half-width, that is $a/2$ and $a_s/2$, respectively. The layups for all of the wingbox components are listed in Table 3. All of the layups consist of $0.125mm$ thick orthotropic plies whose material properties are shown in Table 4. With reference to the loading conditions, the A section of the wingbox (See Fig.9) is considered fully clamped, while a rigid body motion of the B section is prescribed. Namely, the motion of each point of the B section of the wingbox is described with respect to the point located at the section centre. Assuming that the section remains flat during the analysis, the section centre undergoes a transverse displacement along the X_3-axis, $\bar{u}_3 = 0.5\,mm$, and two rotations around the X_1-axis and X_2-axis, $\bar{\vartheta}_1 = \bar{\vartheta}_2 = 0.655 \times 10^{-3}\,rad$. Furthermore a uniform thermal load $\Delta T = 25°K$ is imposed over the skin and the stiffeners' flange. The analysis is conducted with a displacement-control solution procedure. A domain decomposition consisting of 140 plates is considered

and the same order of polynomial approximation for the variables is assumed for all of the plates, namely $N = M = 6$, which gives a total of 30240 DOFs and provides converged results. Finite element analysis was performed with Abaqus, using a mesh with 118540 $S4R$ elements and 150 different layups, for a total of 714843 DOFs, which also provides converged results.

The deformed buckled structure in correspondence at the maximum applied load is depicted in Fig.11, where the contour-map refers to the transverse displacements u_3 normalized with respect to the skin thickness. For the sake of clarity, the same results are shown as an exploded view in Fig.12. These results show that the proposed method can also follow the deep postbuckling response of such structures as, at the maximum applied load, the maximum transverse displacement of the skin's panels is slightly more than twice their thickness. As regards the accuracy of the solution, Fig.13 shows the results in terms of the transverse displacement u_3 versus the applied load factor λ for five reference points of the upper skin of the wingbox whose coordinates are given in Table 5. The transverse displacements are normalized with respect to the skin thickness. For all of these points, the postbuckling equilibrium paths shown in Fig.13 give excellent agreement with finite element results, with negligible difference. Fig.14 shows an exploded view of the wingbox where the contour-map refers to the distribution of the absolute differences between the transverse displacements u_3 of the present solution and the results of the analyses performed with Abaqus. The absolute difference is normalized with respect to the maximum transverse displacement obtained with the finite element analyses. As shown in Fig.14 for the maximum applied load the difference is negligible except in the regions where the influence of the stiffeners runout is significant. However, the maximum difference is limited to $\sim 1.1\%$ for a maximum normalized transverse displacement ${}^{u_3}/_{th} > 2.1$. In Fig.15 the equilibrium path of the point F of the wingbox's bottom skin with coordinates $F\,[-533.9, 472.5, -63.5]$ is shown. The point F is the point that exhibits the maximum difference with respect to FEM analysis results. As shown in Fig.15, the difference between the present and the FEA solution become appreciable only for values of the load factor $\lambda > 0.6$, that

is well after the post-bucking regime begins, and it remains limited ($\sim 1.5\%$ of the skin thickness) up to the maximum applied load.

6. Conclusions

A multidomain Rayleigh-Ritz approach for an assembly of generally restrained multilayered stiffened variable angle tow plates in the post-buckling regime is presented. First-order shear deformation theory, including thermal effects, and large displacement von Kármán assumptions are employed for each element of the domain decomposition, which can represent general layups. Legendre orthogonal polynomials approximate the unknown displacement field and penalty techniques are used to enforce structural continuity of the assembled thin-walled structures as well as the kinematical boundary conditions. The developed approach is used to analyse the postbuckling behaviour of typical airframe composite structures with straight fibre or linear variation of the ply fibre angle along a prescribed direction. The proposed solutions are validated by comparison with literature and finite element analysis and original results are presented for the thermo-mechanical post-buckling solution of multilayered stiffened variable angle tow plates. The developed postbuckling analysis tool is sufficiently versatile to model a wide range of plate configurations and load cases for multi-component laminated composite structures. The excellent properties of Legendre orthogonal polynomials for capturing local responses with few terms allows a significant reduction in the number of unknowns, that is more than 80% for the discussed test cases. Furthermore, the introduced domain decomposition relates to geometrical modelling only, providing simplified data preparation compared to finite element analysis. Results obtained for the postbuckling of VAT stiffened panels show that the present tool can also follow the deep postbuckling response of such structures without loss in the accuracy of the solution. The proposed postbuckling solution for a wingbox structure shows the effectiveness of the analysis tool for complex aerospace structures. For this structure it provides the same accuracy level as finite element analysis,

with the maximum difference in out-of-plane displacements limited to 1.1% of the skin thickness. These results demonstrate the usefulness of the analysis tool for design purposes.

Appendix A. Tangent stiffness matrices

By using Eqs. (26b), (26c) and (26f) and recalling that $\frac{d\boldsymbol{\mathcal{B}}_{nlU}^{\langle k\rangle}\boldsymbol{U}^{\langle k\rangle}}{d\boldsymbol{U}^{\langle k\rangle}} = 2\boldsymbol{\mathcal{B}}_{nlU}^{\langle k\rangle}$, then

$$\begin{aligned}
&\frac{d}{d\boldsymbol{X}^{\langle k\rangle}}\left(\left[\boldsymbol{K}_1^{\langle k\rangle}+\bar{\boldsymbol{K}}_1^{\langle k\rangle}+\boldsymbol{K}_2^{\langle k\rangle}-\boldsymbol{K}_{\Delta T}^{\langle k\rangle}\right]\boldsymbol{X}^{\langle k\rangle}\right) = \\
&\int_{\Omega^{\langle k\rangle}}\begin{bmatrix}\boldsymbol{\mathcal{W}} & {\boldsymbol{\mathcal{B}}_{nlU}^{\langle k\rangle}}^T\boldsymbol{B}^{\langle k\rangle}\boldsymbol{\mathcal{B}}_{p\Theta}^{\langle k\rangle}\\ {\boldsymbol{\mathcal{B}}_{p\Theta}^{\langle k\rangle}}^T\boldsymbol{B}^{\langle k\rangle}\boldsymbol{\mathcal{B}}_{nlU}^{\langle k\rangle} & \boldsymbol{0}\end{bmatrix}d\Omega + \\
&\int_{\Omega^{\langle k\rangle}}\begin{bmatrix}\left(\frac{d\boldsymbol{\mathcal{B}}_{nlU}^{\langle k\rangle}}{d\boldsymbol{U}^{\langle k\rangle}}\right)^T\left[\boldsymbol{A}_p^{\langle k\rangle}\left(\boldsymbol{\mathcal{B}}_{pU}^{\langle k\rangle}+\bar{\boldsymbol{\mathcal{B}}}_{nlU}^{\langle k\rangle}+\frac{1}{2}\boldsymbol{\mathcal{B}}_{nlU}^{\langle k\rangle}\right)-N_{\Delta T}^{\langle k\rangle}\right] & \left(\frac{d\boldsymbol{\mathcal{B}}_{nlU}^{\langle k\rangle}}{d\boldsymbol{U}^{\langle k\rangle}}\right)^T\boldsymbol{B}^{\langle k\rangle}\boldsymbol{\mathcal{B}}_{p\Theta}^{\langle k\rangle}\\ \boldsymbol{0} & \boldsymbol{0}\end{bmatrix}d\Omega\begin{Bmatrix}\boldsymbol{U}^{\langle k\rangle}\\ \boldsymbol{\Theta}^{\langle k\rangle}\end{Bmatrix}
\end{aligned} \tag{A.1}$$

where

$$\begin{aligned}
\boldsymbol{\mathcal{W}} =& {\boldsymbol{\mathcal{B}}_{pU}^{\langle k\rangle}}^T\boldsymbol{A}_p^{\langle k\rangle}\boldsymbol{\mathcal{B}}_{nlU}^{\langle k\rangle}+{\boldsymbol{\mathcal{B}}_{nlU}^{\langle k\rangle}}^T\boldsymbol{A}_p^{\langle k\rangle}\left(\boldsymbol{\mathcal{B}}_{pU}^{\langle k\rangle}+\boldsymbol{\mathcal{B}}_{nlU}^{\langle k\rangle}+\bar{\boldsymbol{\mathcal{B}}}_{nlU}^{\langle k\rangle}\right)+{\bar{\boldsymbol{\mathcal{B}}}_{nlU}^{\langle k\rangle}}^T\boldsymbol{A}_p^{\langle k\rangle}\boldsymbol{\mathcal{B}}_{nlU}^{\langle k\rangle} \\
&-{\boldsymbol{\mathcal{B}}_{nU}^{\langle k\rangle}}^T\widehat{\boldsymbol{N}}_{\Delta T}^{\langle k\rangle}\boldsymbol{\mathcal{B}}_{nU}^{\langle k\rangle}
\end{aligned} \tag{A.2}$$

From Eq. (11) one gets

$$\left(\frac{d\boldsymbol{\mathcal{B}}_{nlU}^{\langle k\rangle}}{d\boldsymbol{U}^{\langle k\rangle}}\right)^T\left[\boldsymbol{A}_p^{\langle k\rangle}\left(\boldsymbol{\mathcal{B}}_{pU}^{\langle k\rangle}+\bar{\boldsymbol{\mathcal{B}}}_{nlU}^{\langle k\rangle}+\frac{1}{2}\boldsymbol{\mathcal{B}}_{nlU}^{\langle k\rangle}\right)\boldsymbol{U}^{\langle k\rangle}-N_{\Delta T}^{\langle k\rangle}+\boldsymbol{B}^{\langle k\rangle}\boldsymbol{\mathcal{B}}_{p\Theta}^{\langle k\rangle}\boldsymbol{\Theta}^{\langle k\rangle}\right] = \left(\frac{d\boldsymbol{\mathcal{B}}_{nlU}^{\langle k\rangle}}{d\boldsymbol{U}^{\langle k\rangle}}\right)^T\boldsymbol{N}^{\langle k\rangle} \tag{A.3}$$

and, with simple manipulations,

$$\left(\frac{d\boldsymbol{\mathcal{B}}_{nlU}^{\langle k\rangle}}{d\boldsymbol{U}^{\langle k\rangle}}\right)^T\boldsymbol{N}^{\langle k\rangle} = \left(\left[\boldsymbol{\mathscr{D}}_p\otimes\left(\boldsymbol{\Phi}_{u_3}^{\langle k\rangle}\right)\right]\boldsymbol{\mathscr{D}}_n\boldsymbol{\Phi}_u^{\langle k\rangle}\right)^T\boldsymbol{N}^{\langle k\rangle} = {\boldsymbol{\mathcal{B}}_{nU}^{\langle k\rangle}}^T\widehat{\boldsymbol{N}}^{\langle k\rangle}\boldsymbol{\mathcal{B}}_{nU}^{\langle k\rangle} \tag{A.4}$$

where

$$\widehat{\boldsymbol{N}}^{\langle k\rangle} = \begin{bmatrix}N_1^{\langle k\rangle} & N_3^{\langle k\rangle} & 0\\ N_3^{\langle k\rangle} & N_2^{\langle k\rangle} & 0\\ 0 & 0 & 0\end{bmatrix} \tag{A.5}$$

Taking Eqs. (A.3) and (A.4) into account, one finally obtains

$$\frac{d}{d\boldsymbol{X}^{\langle k\rangle}}\Big(\Big[\boldsymbol{K}_1^{\langle k\rangle}+\bar{\boldsymbol{K}}_1^{\langle k\rangle}+\boldsymbol{K}_2^{\langle k\rangle}-\boldsymbol{K}_{\Delta T}^{\langle k\rangle}\Big]\boldsymbol{X}^{\langle k\rangle}\Big)= \int_{\Omega^{\langle k\rangle}}\begin{bmatrix}\boldsymbol{\mathcal{W}}+{\boldsymbol{\mathcal{B}}_{nU}^{\langle k\rangle}}^T\widehat{\boldsymbol{N}}^{\langle k\rangle}\boldsymbol{\mathcal{B}}_{nU}^{\langle k\rangle} & {\boldsymbol{\mathcal{B}}_{nlU}^{\langle k\rangle}}^T\boldsymbol{B}^{\langle k\rangle}\boldsymbol{\mathcal{B}}_{p\Theta}^{\langle k\rangle}\\ {\boldsymbol{\mathcal{B}}_{p\Theta}^{\langle k\rangle}}^T\boldsymbol{B}^{\langle k\rangle}\boldsymbol{\mathcal{B}}_{nlU}^{\langle k\rangle} & \boldsymbol{0}\end{bmatrix}d\Omega= \Big(\boldsymbol{K}_{1t}^{\langle k\rangle}+\bar{\boldsymbol{K}}_{1t}^{\langle k\rangle}+\boldsymbol{K}_{2t}^{\langle k\rangle}-\boldsymbol{K}_{\Delta T}^{\langle k\rangle}+\boldsymbol{K}_{G}^{\langle k\rangle}\Big) \tag{A.6}$$

where

$$\boldsymbol{K}_{1t}^{\langle k\rangle}=\int_\Omega\begin{bmatrix}{\boldsymbol{\mathcal{B}}_{pU}^{\langle k\rangle}}^T\boldsymbol{A}_p^{\langle k\rangle}\boldsymbol{\mathcal{B}}_{nlU}^{\langle k\rangle}+{\boldsymbol{\mathcal{B}}_{nlU}^{\langle k\rangle}}^T\boldsymbol{A}_p^{\langle k\rangle}\boldsymbol{\mathcal{B}}_{pU}^{\langle k\rangle} & {\boldsymbol{\mathcal{B}}_{nlU}^{\langle k\rangle}}^T\boldsymbol{B}^{\langle k\rangle}\boldsymbol{\mathcal{B}}_{p\Theta}^{\langle k\rangle}\\ {\boldsymbol{\mathcal{B}}_{p\Theta}^{\langle k\rangle}}^T\boldsymbol{B}^{\langle k\rangle}\boldsymbol{\mathcal{B}}_{nlU}^{\langle k\rangle} & \boldsymbol{0}\end{bmatrix}d\Omega \tag{A.7a}$$

$$\bar{\boldsymbol{K}}_{1t}^{\langle k\rangle}=\int_\Omega\begin{bmatrix}{\boldsymbol{\mathcal{B}}_{nlU}^{\langle k\rangle}}^T\boldsymbol{A}_p^{\langle k\rangle}\bar{\boldsymbol{\mathcal{B}}}_{nlU}^{\langle k\rangle}+{\bar{\boldsymbol{\mathcal{B}}}_{nlU}^{\langle k\rangle}}^T\boldsymbol{A}_p^{\langle k\rangle}\boldsymbol{\mathcal{B}}_{nlU}^{\langle k\rangle} & \boldsymbol{0}\\ \boldsymbol{0} & \boldsymbol{0}\end{bmatrix}d\Omega \tag{A.7b}$$

$$\boldsymbol{K}_{2t}^{\langle k\rangle}=\int_\Omega\begin{bmatrix}{\boldsymbol{\mathcal{B}}_{nlU}^{\langle k\rangle}}^T\boldsymbol{A}_p^{\langle k\rangle}\boldsymbol{\mathcal{B}}_{nlU}^{\langle k\rangle} & \boldsymbol{0}\\ \boldsymbol{0} & \boldsymbol{0}\end{bmatrix}d\Omega \tag{A.7c}$$

$$\boldsymbol{K}_{G}^{\langle k\rangle}=\int_\Omega\begin{bmatrix}{\boldsymbol{\mathcal{B}}_{nU}^{\langle k\rangle}}^T\widehat{\boldsymbol{N}}^{\langle k\rangle}\boldsymbol{\mathcal{B}}_{nU}^{\langle k\rangle} & \boldsymbol{0}\\ \boldsymbol{0} & \boldsymbol{0}\end{bmatrix}d\Omega \tag{A.7d}$$

Differentiation of Eq. (25), accounting for Eq. (A.6) and considering that all of the other terms linearly depend on the problem variables, provide the incremental form of the governing equations that, for $k=1,\dots,N_P$, read as Eq. (29)

References

[1] M. Hyer, H. Lee, The use of curvilinear fiber format to improve buckling resistance of composite plates with central circular holes, Composite Structures 18 (1991) 239–261.

[2] Z. Gürdal, R. Olmedo, In-plane response of laminates with spatially varying fiber orientations-variable stiffness concept, AIAA Journal 31 (4) (1993) 751–758.

[3] S. Biggers, S. Fageau, Shear buckling response of tailored rectangular composite plates, AIAA Journal 32 (5) (1994) 1100–1103.

[4] A. Leissa, A review of laminated composite plate buckling, Applied Mechanics Reviews 40 (5) (1987) 575–591.

[5] C. Chia, Geometrically nonlinear behavior of composite plates: A review, Applied Mechanics Reviews 41 (12) (1988) 439–451.

[6] G. Turvey, I. Marshall (Eds.), Buckling and postbuckling of composite plates, Springer Netherlands, 1995.

[7] A. K. Noor, J. M. Peters, Buckling and postbuckling analyses of laminated anisotropic structures, International Journal for Numerical Methods in Engineering 27 (2) (1989) 383–401.

[8] E. Cosentino, P. Weaver, Approximate nonlinear analysis method for debonding of skin/stringer composite assemblies, AIAA Journal 46 (5) (2008) 1144–1159.

[9] C. Mittelstedt, Explicit local buckling analysis of stiffened composite plates accounting for periodic boundary conditions and stiffener-plate interaction, Composite Structures 91 (3) (2009) 249–265.

[10] D. Stamatelos, G. Labeas, K. Tserpes, Analytical calculation of local buckling and post-buckling behavior of isotropic and orthotropic stiffened panels, Thin-Walled Structures 49 (3) (2011) 422–430.

[11] L. Brubak, J. Hellesland, Semi-analytical postbuckling analysis of stiffened imperfect plates with a free or stiffened edge, Computers and Structures 89 (17-18) (2011) 1574–1585.

[12] R. Vescovini, C. Bisagni, Two-step procedure for fast post-buckling analysis of composite stiffened panels, Computers and Structures 128 (2013) 38–47.

[13] H. Zheng, Z. Wei, Vibroacoustic analysis of stiffened plates with nonuniform boundary conditions, International Journal of Applied Mechanics 5 (4).

[14] M. M. Saadatpour, M. Azhari, M. A. Bradford, Analysis of general quadrilateral orthotropic thick plates with arbitrary boundary conditions by the Rayleigh Ritz method, International Journal for Numerical Methods in Engineering 54 (7) (2002) 1087–1102.

[15] R. Rango, F. Bellomo, L. Nallim, A general Ritz algorithm for static analysis of arbitrary laminated composite plates using first order shear deformation theory, Journal of Engineering Research 10 (2) (2013) 1–12.

[16] S. Wang, A unified Timoshenko beam b-spline Rayleigh-Ritz method for vibration and buckling analysis of thick and thin beams and plates, International Journal for Numerical Methods in Engineering 40 (3) (1997) 473–491.

[17] K. Liew, Solving the vibration of thick symmetric laminates by Reissner/Mindlin plate theory and the p-Ritz method, Journal of Sound and Vibration 198 (3) (1996) 343–360.

[18] Y. Cheung, D. Zhou, Vibrations of moderately thick rectangular plates in terms of a set of static Timoshenko beam functions, Computers and Structures 78 (6) (2000) 757–768.

[19] D. Zhou, Vibrations of Mindlin rectangular plates with elastically restrained edges using static Timoshenko beam functions with the Rayleigh-Ritz method, International Journal of Solids and Structures 38 (32-33) (2001) 5565–5580.

[20] S. Eftekhar, A. Jafari, A novel and accurate Ritz formulation for free vibration of rectangular and skew plates, Journal of Applied Mechanics, Transactions ASME 79 (6) (2012) art. no 064504 (5 pages).

[21] S. Eftekhari, A. Jafari, A simple and accurate Ritz formulation for free vibration of thick rectangular and skew plates with general boundary conditions, Acta Mechanica 224 (1) (2013) 193–209.

[22] K. Liew, J. Wang, M. Tan, S.Rajendran, Nonlinear analysis of laminated composite plates using the mesh-free kp-Ritz method based on FSDT, Computer Methods in Applied Mechanics and Engineering 193 (45-47) (2004) 4763–4779.

[23] K. Liew, J. Wang, M. Tan, S. Rajendran, Postbuckling analysis of laminated composite plates using the mesh-free kp-Ritz method, Computer Methods in Applied Mechanics and Engineering 195 (7-8) (2006) 551–570.

[24] Y. Lee, X.Zhao, J. Reddy, Postbuckling analysis of functionally graded plates subject to compressive and thermal loads, Computer Methods in Applied Mechanics and Engineering 199 (25-28) (2010) 1645–1653.

[25] A. Ghorbanpour Arani, A. Loghman, A. Mosallaie Barzoki, R. Kolahchi, Elastic buckling analysis of ring and stringer-stiffened cylindrical shells under general pressure and axial compression via the Ritz method, Journal of Solid Mechanics 2 (4) (2010) 332–347.

[26] M. Talebitooti, M. Ghayour, S. Ziaei-Rad, R. Talebitooti, Free vibrations of rotating composite conical shells with stringer and ring stiffeners, Archive of Applied Mechanics 80 (3) (2010) 201–215.

[27] Z. Gürdal, B. Tatting, C. Wu, Variable stiffness composite panels: Effects of stiffness variation on the in-plane and buckling response, Composites Part A: Applied Science and Manufacturing 39 (5) (2008) 911–922.

[28] C. Lopes, Z. Gürdal, P. Camanho, Variable-stiffness composite panels: Buckling and first-ply failure improvements over straight-fibre laminates, Computers and Structures 86 (9) (2008) 897–907.

[29] G. Raju, Z. Wu, B. Kim, P. Weaver, Prebuckling and buckling analysis of variable angle tow plates with general boundary conditions, Composite Structures 94 (9) (2012) 2961–2970.

[30] Z. Wu, P. Weaver, G. Raju, B. Chul Kim, Buckling analysis and optimisation of variable angle tow composite plates, Thin-Walled Structures (163-172) (2012) 60.

[31] Z. Wu, P. Weaver, G. Raju, Postbuckling optimisation of variable angle tow composite plates, Composite Structures 103 (2013) 34–42.

[32] G. Raju, Z. Wu, P. Weaver, Postbuckling analysis of variable angle tow plates using differential quadrature method, Composite Structures 106 (2013) 74–84.

[33] W. Liu, R. Butler, Buckling optimization of variable-angle-tow panels using the infinite-strip method, AIAA Journal 51 (6) (2013) 1442–1449.

[34] Z. Wu, G. Raju, P. Weaver, Postbuckling analysis of variable angle tow composite plates, International Journal of Solids and Structures 50 (10) (2013) 1770–1780.

[35] J. Yang, B. Song, X. Zhong, Parametric study on buckling property of variable angle tow laminates, Fuhe Cailiao Xuebao/Acta Materiae Compositae Sinica 32 (4) (2015) 1145–1152.

[36] G. Raju, Z. Wu, P. Weaver, Buckling and postbuckling of variable angle tow composite plates under in-plane shear loading, International Journal of Solids and Structures 58 (2015) 270–287.

[37] Z. Wu, G. Raju, P. Weaver, Framework for the buckling optimization of variable-angle tow composite plates, AIAA Journal 53 (12) (2015) 3788–3804.

[38] S. C. White, P. M. Weaver, Towards imperfection insensitive buckling response of shell structures-shells with plate-like post-buckled responses, The Aeronautical Journal 120 (1224) (2016) 233–253.

[39] R. Groh, P. Weaver, Buckling analysis of variable angle tow, variable thickness panels with transverse shear effects, Composite Structures 107 (2014) 482–493.

[40] B. H. Coburn, P. M. Weaver, Buckling analysis, design and optimisation of variable-stiffness sandwich panels, International Journal of Solids and Structures 96 (2016) 217 – 228.

[41] B. Coburn, Z. Wu, P. Weaver, Buckling analysis of stiffened variable angle tow panels, Composite Structures 111 (1) (2014) 259–270.

[42] B. H. Coburn, Z. Wu, P. Weaver, Buckling analysis and optimization of blade stiffened variable stiffness panels, in: 56th AIAA/ASCE/AHS/ASC Structures, Structural Dynamics, and Materials Conference, 2015, p. 1438.

[43] A. Milazzo, V. Oliveri, Post-buckling analysis of cracked multilayered composite plates by pb-2 Rayleigh-Ritz method, Composite Structures 132 (2015) 75–86.

[44] V. Oliveri, A. Milazzo, A. Alaimo, Post-buckling analysis of damaged multilayered composite stiffened plates by rayleigh-ritz method, Applied Mechanics and Materials 828 (2016) 99–116.

[45] A. Milazzo, V. Oliveri, Buckling and postbuckling of stiffened composite panels with cracks and delaminations by ritz approach, AIAA Journal (2016) 1–16.

[46] Z. Wu, G. Raju, P. M. Weaver, Comparison of variational, differential quadrature, and approximate closed-form solution methods for buckling of highly flexurally anisotropic laminates., Journal of Engineering Mechanics 139 (8) (2013) 1073 – 1083.

[47] O. C. Zienkiewicz, R. L. Taylor, The Finite Element Method: Solid mechanics, Butterworth-Heinemann, 2002.

[48] J. Reddy, Mechanics of laminated composite plates and shells. Theory and analysis, CRC Press, 2004.

[49] J. Reddy, Energy Principles and Variational Methods in Applied Mechanics, John Wiley & Sons, 2002.

[50] M. A. Crisfield, Non-linear finite element analysis of solids and structures, John Wiley & Sons, 1991.

[51] E. Cosentino, P. Weaver, Prebuckling and buckling of unsymmetrically laminated composite panels with stringer run-outs, AIAA Journal 47 (10) (2009) 2284–2297.

[52] S. Smith, M. Bradford, D. Oehlers, Numerical convergence of simple and orthogonal polynomials for the unilateral plate buckling problem using the Rayleigh-Ritz method, International Journal for Numerical Methods in Engineering 44 (11) (1999) 1685–1707.

[53] J. Yuan, S. Dickinson, Flexural vibration of rectangular plate systems approached by using artificial springs in the Rayleigh-Ritz method, Journal of Sound and Vibration 159 (1) (1992) 39–55.

[54] A. Madeo, R. Groh, G. Zucco, P. Weaver, G. Zagari, R. Zinno, Post-buckling analysis of variable-angle tow composite plates using koiter's approach and the finite element method, Thin-Walled Structures 110 (2017) 1 – 13.

[55] S. Nagendra, Z. Grdal, R. Haftka, J. Starnes, Buckling and failure characteristics of compression-loaded stiffened composite panels with a hole, Composite Structures 28 (1) (1994) 1 – 17.

[56] S. Nagendra, D. Jestin, Z. Grdal, R. Haftka, L. Watson, Improved genetic algorithm for the design of stiffened composite panels, Computers & Structures 58 (3) (1996) 543 – 555.

[57] J. E. Herencia, P. M. Weaver, M. I. Friswell, Optimization of long anisotropic laminated fiber composite panels with t-shaped stiffeners, AIAA Journal 45 (10) (2007) 2497 – 2509.

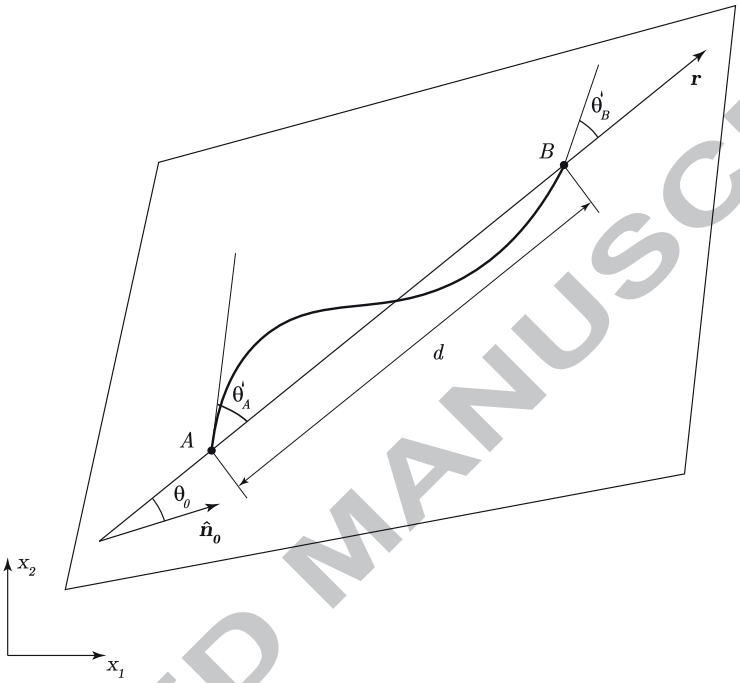

Figure 1: Fibre orientation angle definitions

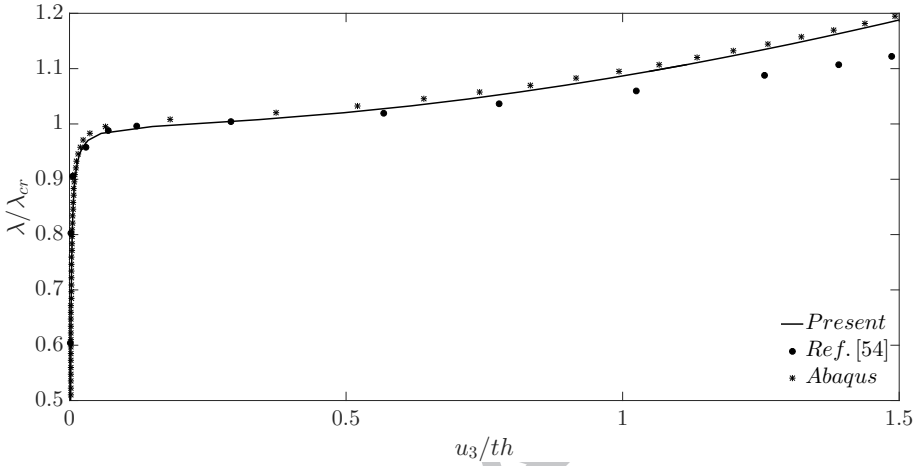

Figure 2: Transverse displacement of $TC1$ square composite VAT plate subjected to uniform axial compression

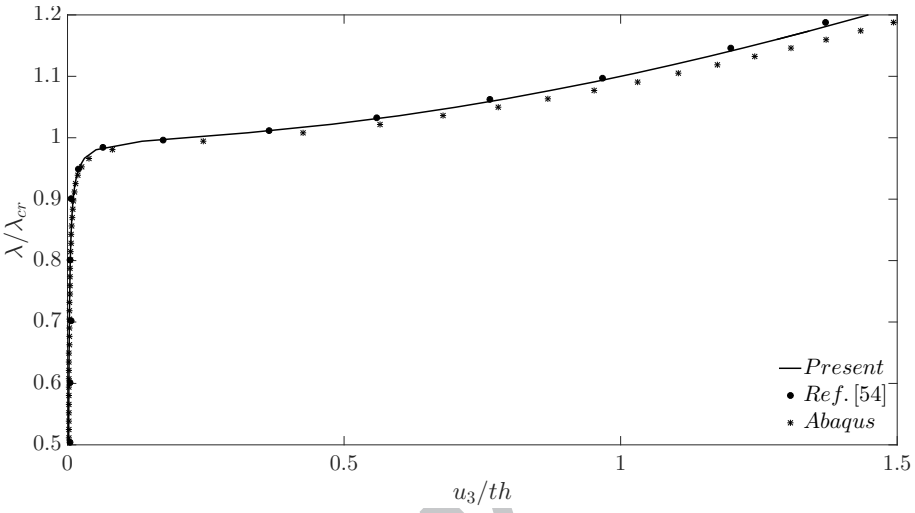

Figure 3: Transverse displacement of $TC2$ square composite VAT plate subjected to biaxial compression

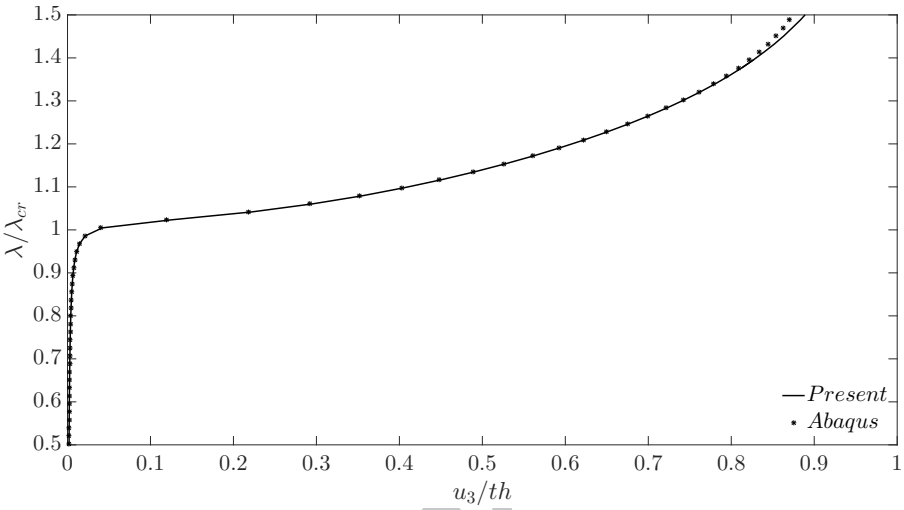

Figure 4: Transverse displacement of $TC3$ square composite VAT plate subjected to uniform change in temperature

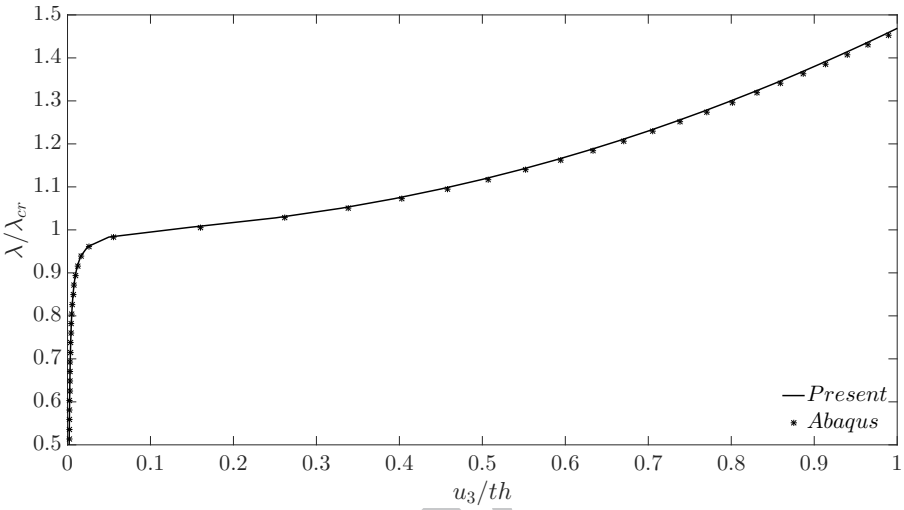

Figure 5: Transverse displacement of $TC4$ square composite VAT plate subjected to uniform change in temperature

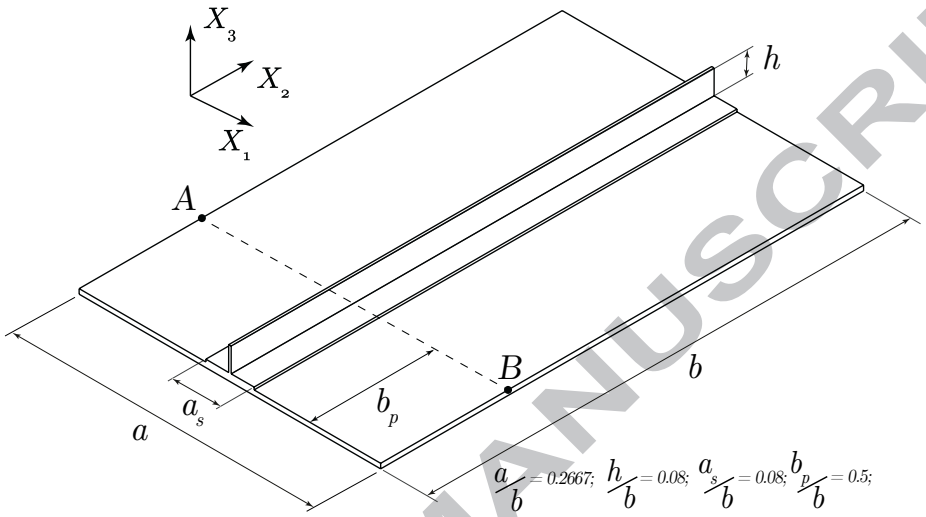

Figure 6: Geometry of stiffened composite VAT plate

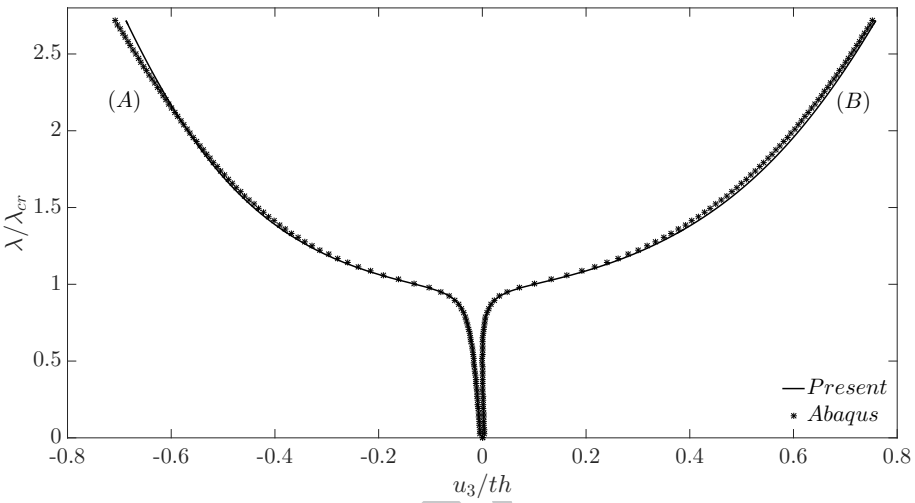

Figure 7: Postbuckling behaviour of stiffened VAT plate subjected to uniaxial compression and uniform thermal load

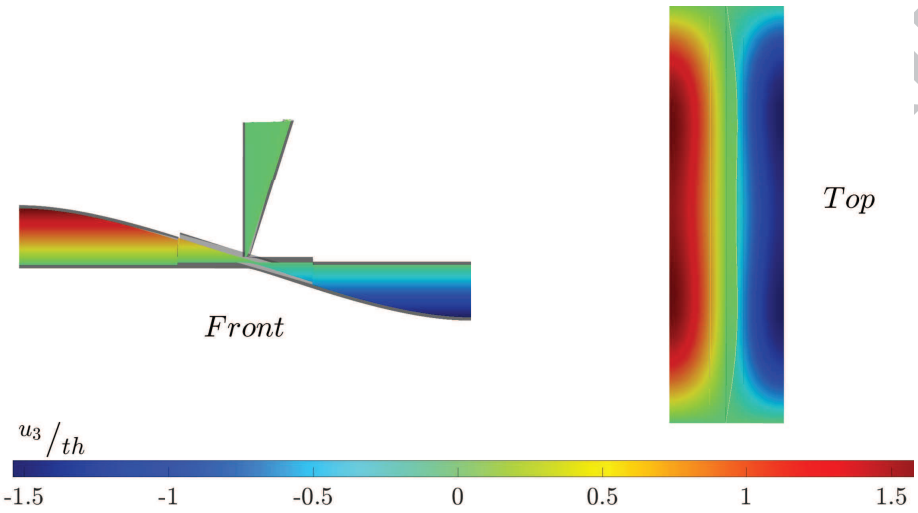

Figure 8: Transverse displacements of stiffened VAT plate subjected to uniaxial compression and uniform thermal load

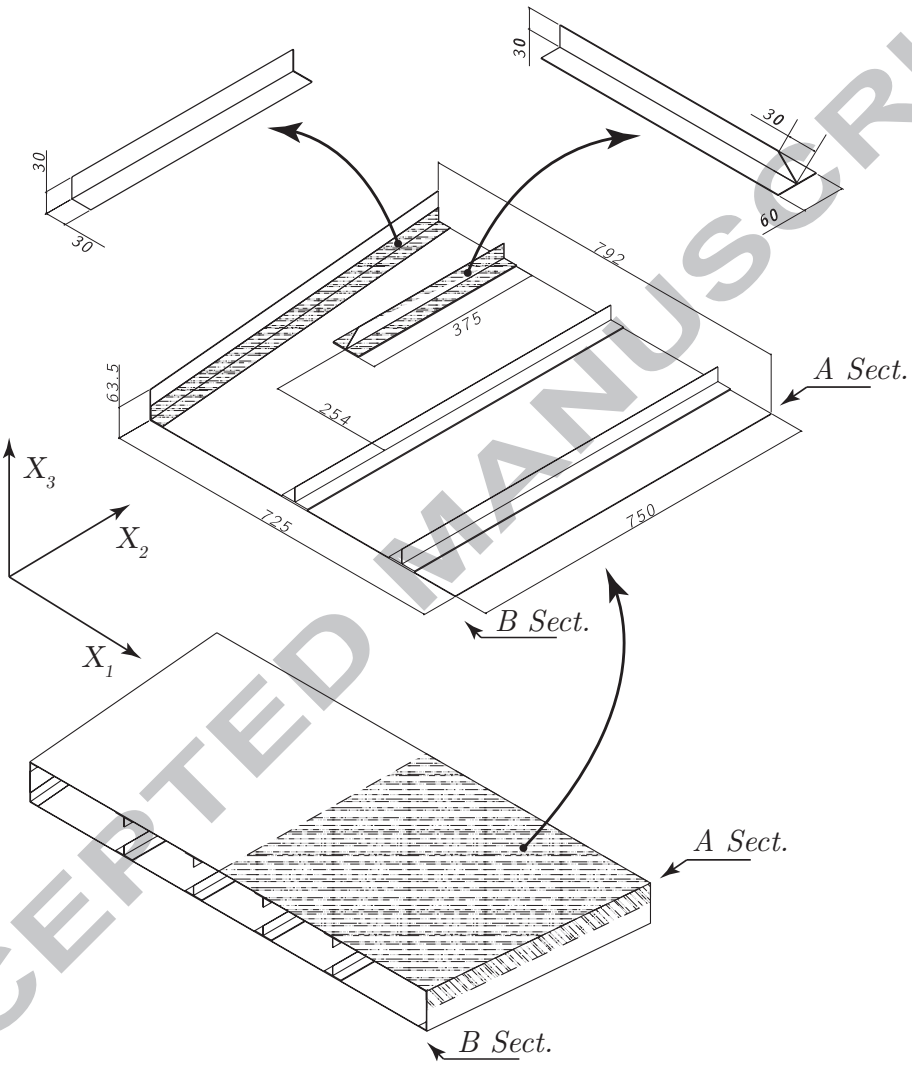

Figure 9: Geometry of the wing-box structure; all dimensions in *mm*

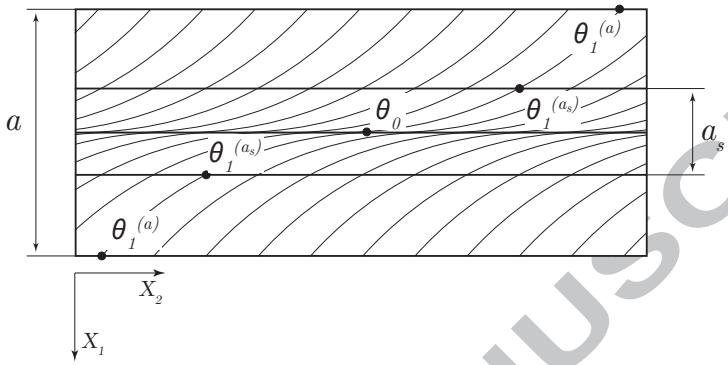

Figure 10: Fibre variation angle definition for the skin and stiffeners' flange

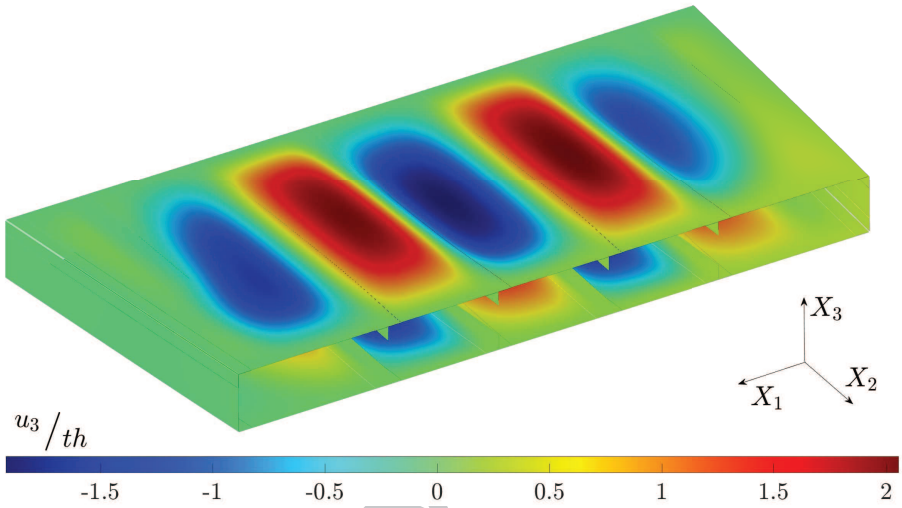

Figure 11: Maximum transverse displacements

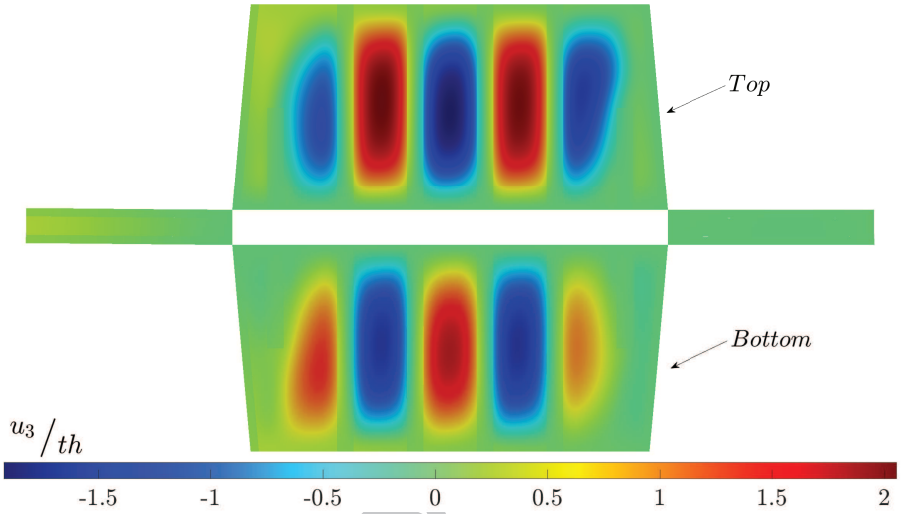

Figure 12: Exploded view of maximum transverse displacements

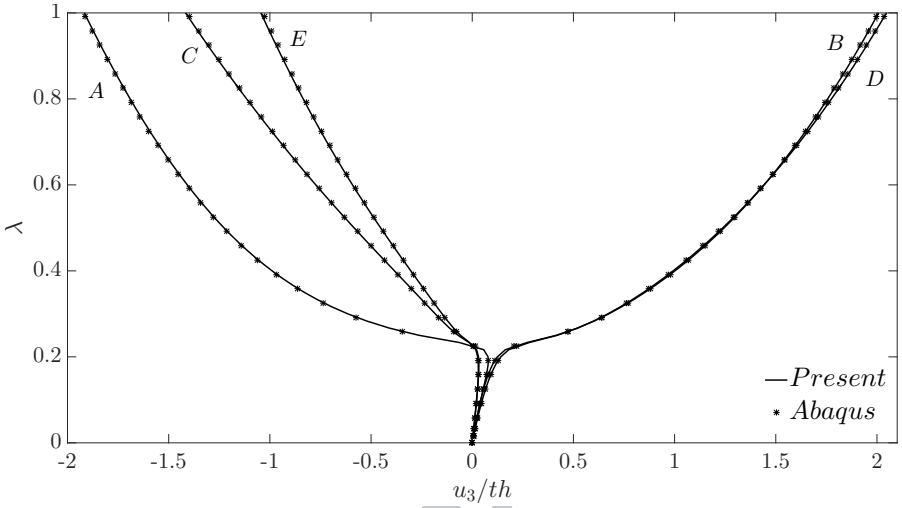

Figure 13: Postbuckling equilibrium path of wingbox's reference points

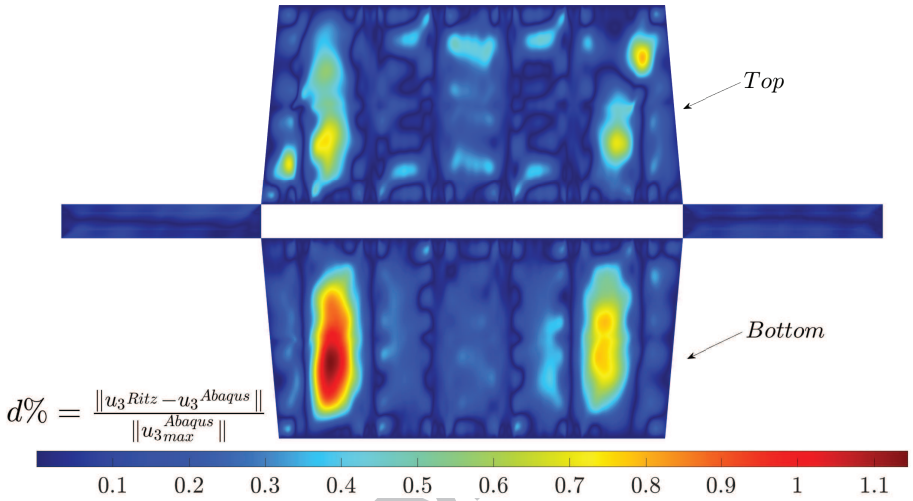

Figure 14: Exploded view of maximum transverse displacement difference with respect to Abaqus

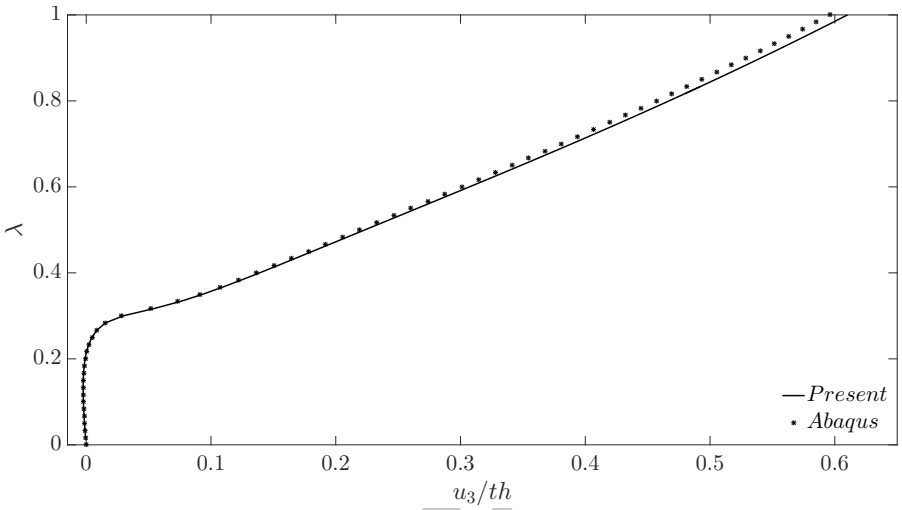

Figure 15: Postbuckling equilibrium path of point F

Table 1: Layups for skin and stiffener of the VAT panel.

Skin	Stiffener flange	Stiffener web
$[0 \pm \langle 0\vert 45\rangle]_6$	$[0 \pm \langle 0\vert 13.5\rangle]_{2_S}$	$[0 \pm \langle\langle 45\vert 0\rangle\rangle]_{2_S}$

Table 2: Material properties.

E_1/E_2	G_{12}/E_2	G_{23}/E_2	G_{31}/E_2	ν_{12}	α_1/α_2
25.0	0.5	0.2	0.5	0.25	-4.4×10^{-3}

Table 3: Layups of wingbox's elements.

Upper and Lower Skin	Tee Stiffener Flange	Tee Stiffener Web	Angle Stiffener	Lateral Skin
$[0 \pm \langle 90 \vert 45 \rangle]_{3_S}$	$[0 \pm \langle 90 \vert 79.37 \rangle]_{2_S}$	$[90]_8$	$[\pm 45]_{2_S}$	$[\pm 45]_{3_S}$

Table 4: Ply material properties for the wingbox.

E_1 $[GPa]$	E_2 $[GPa]$	G_{12} $[GPa]$	G_{23} $[GPa]$	G_{31} $[GPa]$	ν_{12}	α_1 $[\mu\varepsilon/K]$	α_2 $[\mu\varepsilon/K]$
163.0	11.38	5.17	3.98	5.17	0.32	-0.11	25.2

Table 5: Wingbox's reference points.

	X_1	X_2	X_3
A	-508.0	375.0	127.0
B	-254.0	375.0	127.0
C	0.0	375.0	127.0
D	254.0	375.0	127.0
E	508.0	375.0	127.0